Bioactive Materials 49 (2025) 486–501

Contents lists available at ScienceDirect

Bioactive Materials

journal homepage: www.keaipublishing.com/en/journals/bioactive-materials

End-tail soaking strategy toward robust and biomimetic sandwich-layered hydrogels for full-thickness bone regeneration

Jianyang Shan [a,b,1], Liang Cheng [a,1], Xiang Li [a], Wenhao Liu [a,d], Zhihua Liu [a,d], Yimin Chai [a], Yaling Yu [a,*], Xing Wang [b,c,**], Gen Wen [a,***]

[a] Department of Orthopedic Surgery, Shanghai Sixth People's Hospital Affiliated to Shanghai Jiao Tong University School of Medicine, National Center for Orthopaedic Medicine, Shanghai, 200233, China
[b] Beijing National Laboratory for Molecular Sciences, Institute of Chemistry, Chinese Academy of Sciences, Beijing, 100190, China
[c] University of Chinese Academy of Sciences, Beijing, 100049, China
[d] Shanghai Ocean University, College of Fisheries and Life Science, Shanghai, 201306, China

A B S T R A C T

Despite an increasing number of tissue-engineered scaffolds have been developing for bone regeneration, simple and universal fabrication of biomimetic bone microstructure to repair full-thickness bone defects remains a challenge and an acute clinical demand due to the negligence of microstructural differences within the cortex of cancellous bone. In this work, a biomimetic sandwich-layered PACG-CS@Mn(III) hydrogel (SL hydrogel) was facilely fabricated in an end-tail soaking strategy by simply post-crosslinking of poly(acryloyl 2-glycine)-chitosan (PACG-CS) composite hydrogel using trivalent manganese solutions. Taking the merits of *in-situ* formation and flexible adjustment of chain entanglements, hydrogen bonds and metal chelate interactions, SL hydrogel with sandwich-like three-layered structures and anisotropic mechanical performance was easily customized through control of the manganese concentration and soaking time in fore-and-aft sides, simulating the structurally and mechanically biomimetic characteristics of cortical and cancellous bone. Furthermore, the produced SL hydrogel also demonstrated favorable biocompatibility and enhanced MnSOD activity via a peroxidase-like reaction, which enabled the excellent radical scavenging efficiency and anti-inflammatory regulation for facilitating the activity, proliferation and osteogenic differentiation of bone marrow mesenchymal stem cells (BMSCs). *In vivo* studies further revealed that these SL hydrogels achieved restrictive pro-vascular regeneration through their stratified structure, thereby promoting the differentiation of osteoblasts. Simultaneously, the mechanical cues of stratified structure could mediate macrophage phenotype transitions in accordance with stem cell-osteoblast differentiation process via the PI3K-AKT pathway, resulting in robust osteogenesis and high-quality bone reconstruction. This facile yet efficient strategy of turning anisotropic hydrogel offers a promising alternative for full-thickness repair of bone defects, which is also significantly imperative to achieve high-performance scaffolds with specific usage requirements and expand their clinic applicability in more complex anisotropic tissues.

1. Introduction

Bone defects frequently cause severe pain and disability, necessitating medical treatments like autografts, allografts or synthetic grafts [1,2]. Artificial bone grafts such as hydroxyapatite and calcium phosphate offer alternatives to natural bone-derived grafts for avoiding burdensome issues of donor site damages and insufficient donor materials [3]. However, these artificial grafts still have limitations in osteoconductivity and osseointegration, which drives ongoing research into bioactive bone grafts with mimetic extracellular matrix (ECM) features [4–6]. It is well known that bone ECM is composed of cross-linked collagen protofibrils in a highly ordered and interlaced manner with typical micro- and nanoscale hierarchical structures and anisotropic mechanics, which is significantly important on the cell proliferation, migration, aggregation and secretion as well as the bone regeneration [7–9]. Bone has a complex hierarchical structure to regulate various cells, including immune cells, bone marrow mesenchymal stem cells, nerve cells, and endothelial cells [10]. The microstructure of bone is actually not a simple layered structure. On the contrary, the twisted arrangement of needle and plate mineral particles at different levels forms macro-structures of different strengths, which requires optimize combination of stiffness and toughness for full-layer bone repair while

Peer review under the responsibility of KeAi Communications Co., Ltd.
* Corresponding author.
** Corresponding author. Beijing National Laboratory for Molecular Sciences, Institute of Chemistry, Chinese Academy of Sciences, Beijing, 100190, China.
*** Corresponding author.
E-mail addresses: ylingyu@sjtu.edu.cn (Y. Yu), wangxing@iccas.ac.cn (X. Wang), wengen2006@126.com (G. Wen).
[1] These authors contributed equally to this work.

https://doi.org/10.1016/j.bioactmat.2025.02.045
Received 18 October 2024; Received in revised form 10 February 2025; Accepted 28 February 2025

considering its multi-layer tissue structure [11]. Natural lamellar bone consists of dense cortical bone and spongy cancellous bone. Cortical bone has an anisotropic lamellar structure with high mechanical strength [12,13], whereas cancellous bone, often limited by the bone marrow and other structures, comprises homogeneous porous structures that support bone metabolism and hematopoiesis [14]. Physical and mechanical characteristics within different layers have a synergistic effect on immune response, angiogenesis and osteogenesis during bone healing, suggesting an advantage of bone grafts with appropriate biomimetic features [15–18]. Numerous materials related to bone regeneration have been designed and developed for the simulation of multilayered bone structures [19,20]. Although these scaffolds are capable of accelerating bone healing and post-osteogenic function, no single structure is flexible enough to allow for multiple layers. In addition, a vast majority of layered scaffolds are generally formed by crosslinking or bonding between different layers via the complicated methods [21,22], indicating the facile construction of multilayered architectures to simultaneously mimic cortical and cancellous bone tissues within a single scaffold remains challenging.

Hydrogels have gained considerable attention as an ideal tissue-engineered scaffold because of their excellent biocompatibility, high water content and appropriate mechanical compatibility with tissues for bone regeneration [8,23–27]. Nevertheless, most traditional hydrogels are synthesized with a loose crosslinking and unordered network structure, resulting in poor mechanical properties. The advent of double-network (DN) hydrogel has brought tremendous progress in mechanical performance and potential possibilities for load-bearing tissues. However, due to lack of anisotropic hierarchical structures and biological activity, most of these DN hydrogels are still inadequate compared to that of natural tissues, thus greatly limiting their application in bone tissue engineering and regenerative medicine.

Despite an increasing number of anisotropic hydrogels with multilayered structures and strong mechanical properties have been prepared via the directional freezing, modular assembly (i.e., magnetic or electric field self-assembly), and mechanical cutting techniques for osteochondral tissue engineering [28–32], these currently used methods for constructing multilayered hydrogels are usually complex and cannot achieve universal production. In addition, the interfaces of these tissue-engineered scaffolds between different layers are always not continuous or hard, thereby hindering the optimal repair of bone tissue. Besides, although there are multilayered hydrogel scaffolds with excellent mechanical properties comparable to those of biological tissues, their biocompatibility and biosafety is limited [33–37]. Therefore, it still faces limitations and challenges to simultaneously manufacture strong, tough, biocompatible and accessible hydrogel scaffolds with multilayered hierarchical structures and excellent osteogenic bioactivity using a generic and facile approach for full-thickness bone regeneration.

Manganese plays multiple roles in the process of osteogenesis, including increasing bone mass, promoting stem cell osteogenic differentiation, and mediating immune-mediated osteogenesis [38–40]. The diversity of manganese valence states determines its various roles in biological activities. For example, divalent manganese plays a role in osteogenesis, trivalent manganese participates in redox reactions [41], and tetravalent manganese found in manganese dioxide is active in catalytic reactions [42]. The primary active form of trivalent manganese (Mn(III)) in cells is SOD2 (MnSOD), a crucial component of the antioxidant enzyme system in biological systems [43]. Due to its unique ligand structure and efficient transition metal sites, SOD2 has been extensively studied for catalytic clearance of reactive oxygen species (ROS) in various diseases, particularly in stem cells for bone repair [41]. So, flexible manipulation of the manganese valence states in various regions and duration time is imperative to achieve biological anisotropic scaffolds to promote bone regeneration.

Here, a stepwise end-tail soaking strategy was developed to produce a kind of sandwich-layered hydrogel (SL hydrogel) via simply post-crosslinking of poly (acryloyl 2-glycine)-chitosan (PACG-CS) composite hydrogel into manganese acetate solutions for full-thickness bone repair. PACG–CS hydrogel was firstly prepared by ultraviolet (UV) triggered polymerization of ACG with an embedded short-chain CS, and then converted to distinctive SL hydrogel (top/down: chelation–covalent PACG-CS@Mn(III) DN hydrogel; middle: PACG-CS composite hydrogel) after stepwise end-tail in a manganese acetate solution, similar to the stratified structures of the natural skull (Scheme 1). Crucially, rational regulation of noncovalent interactions and thereby the conformation of polymeric chains can flexibly adjust their structures and mechanics. *In vitro* experiments showed these specific sandwich-layered hydrogels exhibited excellent biocompatibility, favorable cell adhesion and anticipated antioxidant stress through a peroxidase-like reaction, which significantly promoted the macrophage M2 phenotype transition, angiogenesis and osteogenesis via the PI3K-AKT pathway [44,45]. *In vitro* studies also revealed that SL hydrogels regulated an osteoblast-centered immune microenvironment, greatly enriching theoretical understanding of influence of biomaterial scaffolds on local immune environments. *In vivo* calvarial defects were further established to demonstrate the regenerative outcome of SL hydrogel scaffolds, with higher quality of newly formed bone compared to the control and non-layered PACG-CS scaffold without hierarchical characteristics of cortical and cancellous tissues. More importantly, another key advantage of sandwich-layer scaffold was that manganese coordination intervention and the resultant tight upper and lower networks had a vascular-restrictive growth effect, thus enabling the hierarchical repair and regeneration of cortical bone and trabecular bone. Overall, this finding highlights the potential of sandwich-layered scaffolds for full-thickness regeneration of calvarial defects, and the combination of hierarchical layers with exceptional osteogenic bioactivity in a simple soaking approach could greatly enhance the repair quality of bone defects.

2. Results and discussion

2.1. Characterization of shell-structured PACG-CS@Mn(III) DN hydrogels

As shown in Fig. 1a, PACG-CS@Mn(III) DN hydrogels were simply prepared via UV-initiated free radical polymerization of ACG monomer (Fig. S1) and subsequently immersing it into the manganese acetate solutions for 1 h. During the soaking process, acetate and manganese were gradually permeated into the PACG-CS hydrogel and served as physical crosslinkers to form amino-anion and carboxyl-cations domains, respectively. On the one hand, acetate triggered the salting-out of polymers to drive the spontaneous collapse of short CS chains to form the chain-entanglement network; on the other hand, strong carboxyl/Mn(III) chelation interaction induced to the conversion of polymer aggregation to yield a three-dimensional valent bonding structure, which could tightly hold with carboxyl groups to form the dense polymeric networks. Owing to the gradient concentration of manganese, an outside-in growth was proceeded to form a hydrogel with two distinct layers that of a soft core surrounded by a stiff shell, thus constructing a shell-structured PACG-CS@Mn(III) DN hydrogel with excellent stability and divergent performance. Compared to PACG-CS composite hydrogel, the produced DN hydrogels soaked with manganese acetate at various concentrations (50 mM, 100 mM and 200 mM) were named PACG-CS@Mn50, PACG-CS@Mn100 and PACG-CS@Mn200 DN hydrogels, respectively.

The typical carbonyl (C=O) absorption peak at 1739 cm^{-1} was gradually flatten along with the increased concentration of Mn(III) in FTIR spectra (Fig. 1b), which ascribed to the growing amount of carboxyl/Mn(III) complexation. To confirm the valence state of manganese in the hydrogel due to the possible disproportionation reaction, XPS analysis on the hydrogel's outer shell was performed in Fig. 1c. Two distinct energy levels of manganese were detected in the hydrogel, and further fine spectrum scanning of Mn3s was allowed to determine the

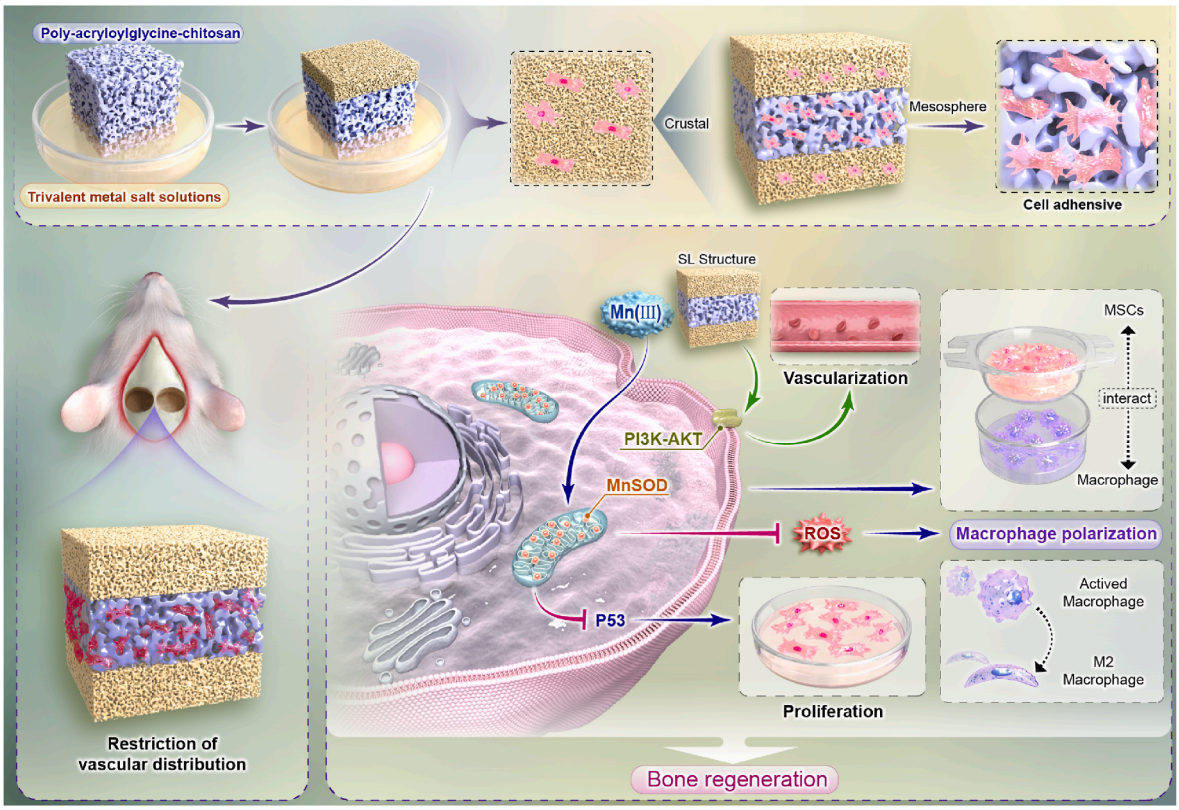

Scheme 1. Schematic illustration of the preparation of biomimetic sandwich-layered hydrogel and its promotion mechanism of bone regeneration.

valence state of chelated manganese (Fig. 1d). Two prominent peaks at 84.7 eV and 90.5 eV, with a peak spacing between 5.3 eV and 6 eV [46], confirmed the predominant existence of trivalent manganese state in the hydrogel. On account of the optimal PACG/CS ratio and gelation conditions in our previous findings, the PACG-CS-1.6 composite hydrogel exhibited a regular alternating "transverse-longitudinal" arrangement (Fig. 1e), which could be attributed to the synergistic effects of chain entanglement, electrostatic adsorption, and hydrogen bonding between cationic CS chains and anionic PACG chains [47]. Therefore, the PACG introduction and multiple physical interactions collaboratively achieved the microstructural variation after formulation optimization, thus contributing to the well-defined hydrogel network with regular arrangement orientation. Along with the gradient diffusion of Mn(III) from the surrounding solution into the gel matrix and interacted with the carboxyl groups, a shell-structured network was consequently formed and grew in a radial direction inward from the surface. The pore size of shell layer in the 50 mM immersion solution was significantly larger than that in the 100 mM and 200 mM immersion solutions. It was because under the same conditions, a higher concentration of manganese acetate solution could lead to stronger chelation and denser crosslinking structures, thereby resulting in a more compact shell layer. However, since the concentration of manganese ions was much lower than the concentration of carboxyl groups in PACG, so there were no significant statistical differences in pore size. It was observed that there were an amount of small tridentate-like reticulation structures in high magnification SEM image of outer shell (Fig. S2), manifesting the strong chelation of PACG with Mn(III). Although the Mn(III) chelated with three carboxyl groups had no visual evidence with the formation of tridentate-like reticulation structures due to various molecular levels, this strong tridentate coordination may play important roles in inducing the orientation arrangement of specific architectures [35,47]. Crucially, the shell layer thickness was closely related to the manganese acetate concentration and immersion time. For example, as shown in Fig. S3a, when the soaking time was extended from 0.5 h to 1 h, the shell microstructures of PACG-CS@Mn100 hydrogels gradually became denser and the pores became smaller. However, further extension of soaking time from 1 h to 4 h had no significant effect on the network microstructures of DN hydrogels, which was mainly due to the concentration of manganese ions was much lower than the concentration of carboxyl groups in PACG. Under this circumstance, PACG-CS@Mn100 DN hydrogels could basically reach the equilibrium state and maintain the stability after soaking for 1 h. Additionally, N_2 adsorption isotherms revealed differential pore size distribution in the hydrogels before and after soaking (Fig. 1f). Consistent with the SEM results, shell-structured PACG-CS@Mn(III) DN hydrogels exhibited variations in pore size distribution.

The typical stress-strain behaviors were further performed to quantitatively examine the mechanical properties of PACG-CS@Mn(III) DN hydrogel after immersing it into the manganese acetate solutions. Compared to the PACG-CS hydrogel, the higher strength and stiffness of PACG-CS@Mn(III) DN hydrogel ascribed to the generated physical chains-entanglements network and coordination interactions between metal ions and carboxyl groups. The hydrogels could achieve a compression stress exceeding 60 MPa at 95 % strain even under low immersion concentration compared to that of PACG-CS hydrogel (ca. 40 MPa, Fig. 1g and Fig. S4a). This strengthening behavior was primarily attributed to the denser and stiffer shell structures on the gel's surface. It was noted that the observation of wobbly points in the compression curves was due to the rupture of shell structures under large deformation, which was also account for the improved tensile strength and modulus (Fig. 1h). Also, rheological measurements provided strong evidences on the remarkable mechanical properties (Fig. S4b). Consistent with the structural variations, the mechanical strength of PACG-CS@Mn100 DN hydrogel soaked for 1 h was also significantly higher than that soaked for 0.5 h, but further extension of time had little change (Fig. S3b).

The manganese concentrations within the PACG-CS@Mn50, PACG-CS@Mn100 and PACG-CS@Mn200 DN hydrogels were actually lower

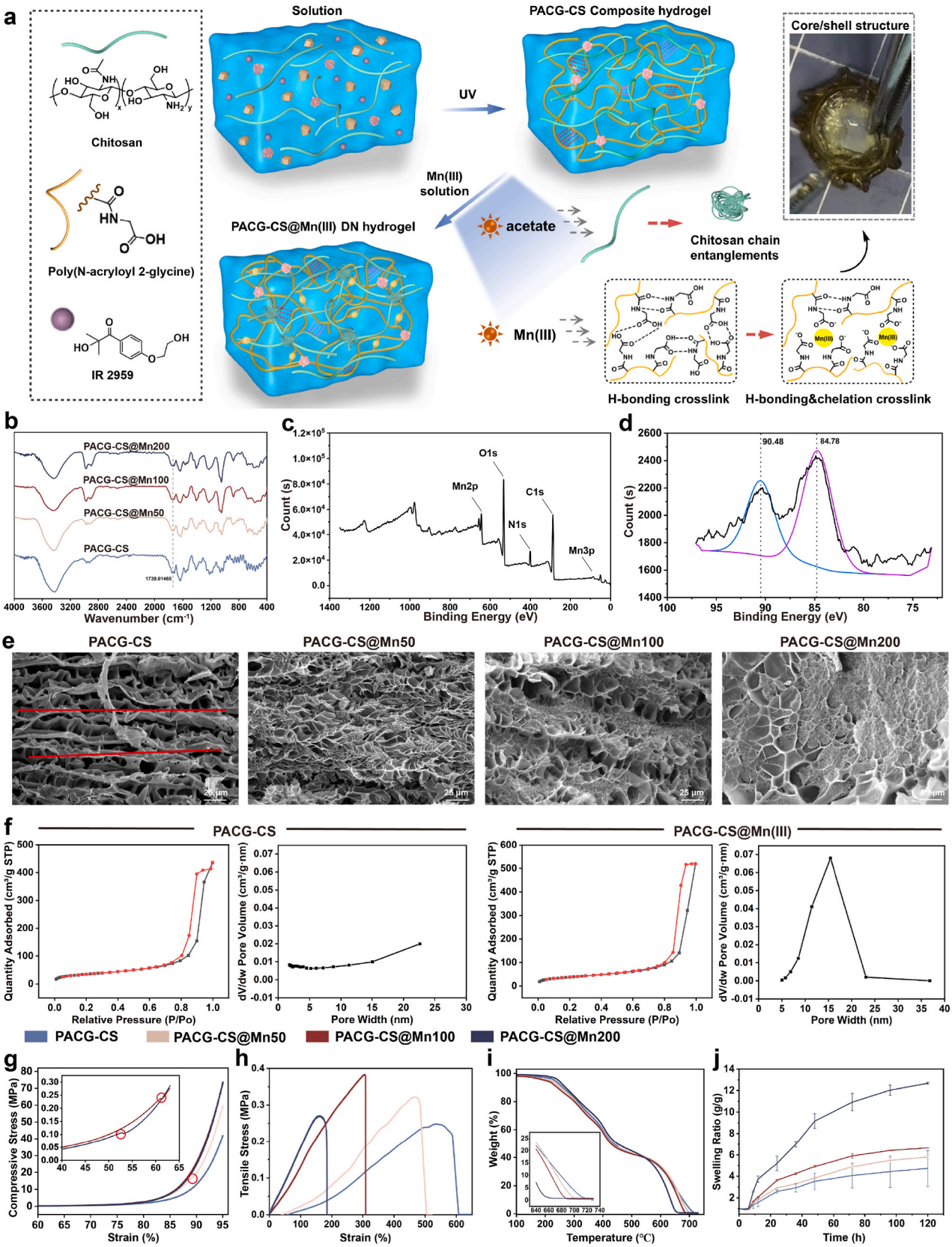

Fig. 1. Fabrication and characterization of PACG-CS composite hydrogel and shell-structured PACG-CS@Mn(III) DN hydrogels. (a) Schematic preparation process of the shell-structured DN hydrogel via an ion soaking method. (b) FTIR spectra of the PACG-CS composite hydrogel and various DN hydrogels. (c, d) XPS full spectrum scans and Mn3s refined spectrum scans of the DN hydrogels. (e) SEM images of composite hydrogel and various DN hydrogels (longitudinal section). (f) N_2-Sorption isotherm image and basic pore size map of the hydrogels. (g–j) Compressive stress-strain curves, tensile stress-strain curves, thermogravimetric analysis curves and *in vitro* swelling behaviors of composite hydrogel and various DN hydrogels.

(0.13 wt%, 0.24 wt% and 0.3 wt%), as verified by the thermogravimetric analysis (TGA) measurement (Fig. 1i) and energy dispersive spectrometer (EDS) analysis (Table S1). However, low concentration of Mn(III) and insufficient amount of carboxyl/Mn(III) complexation was not capable of maintaining structural and mechanical stability after hydrogel swelling in water. So, the gradual release of chelated Mn(III) from the hydrogel could significantly impair the outer hard layer and increase the swelling equilibrium value than that of PACG-CS composite hydrogel (Fig. 1j).

2.2. *In vitro* biocompatibility and degradability

Since the naturally-derived chitosan, glycine derivative and low concentration of manganese were extensively used in tissue engineering and regenerative medicine, the PACG-CS@Mn(III) hydrogels were supposed to be safe and non-toxic. The cytotoxicity was assessed using live-dead staining and CCK-8 methods [48]. On the first day, a small number of bone marrow mesenchymal stem cells (BMSCs) were observed to colonize the hydrogel surface without any dead cells. By the third day, the living cell number was significantly increased with clear observation of high BMSCs viability (Fig. 2a). Cell proliferation viability assays quantitatively demonstrated the high cell survival rate and excellent biocompatibility of these hydrogels regardless of the manganese concentration (Fig. 2b). Similar biocompatibility assessments were verified using the angiogenesis-associated human umbilical vein endothelial cells (HUVEC) and mouse fibroblasts cells (L929), but the hydrogel's cytotoxicity varied with the manganese concentration (Fig. 2c–e). It was worth noting that the proliferation ability of PACG-CS@Mn50 and PACG-CS@Mn200 groups was significantly lower than that of PACG-CS@Mn100 group, which may ascribe to the negligible pro-proliferative effect for the PACG-CS@Mn50 group and excessive cytotoxicity of high manganese concentration for the PACG-CS@Mn200

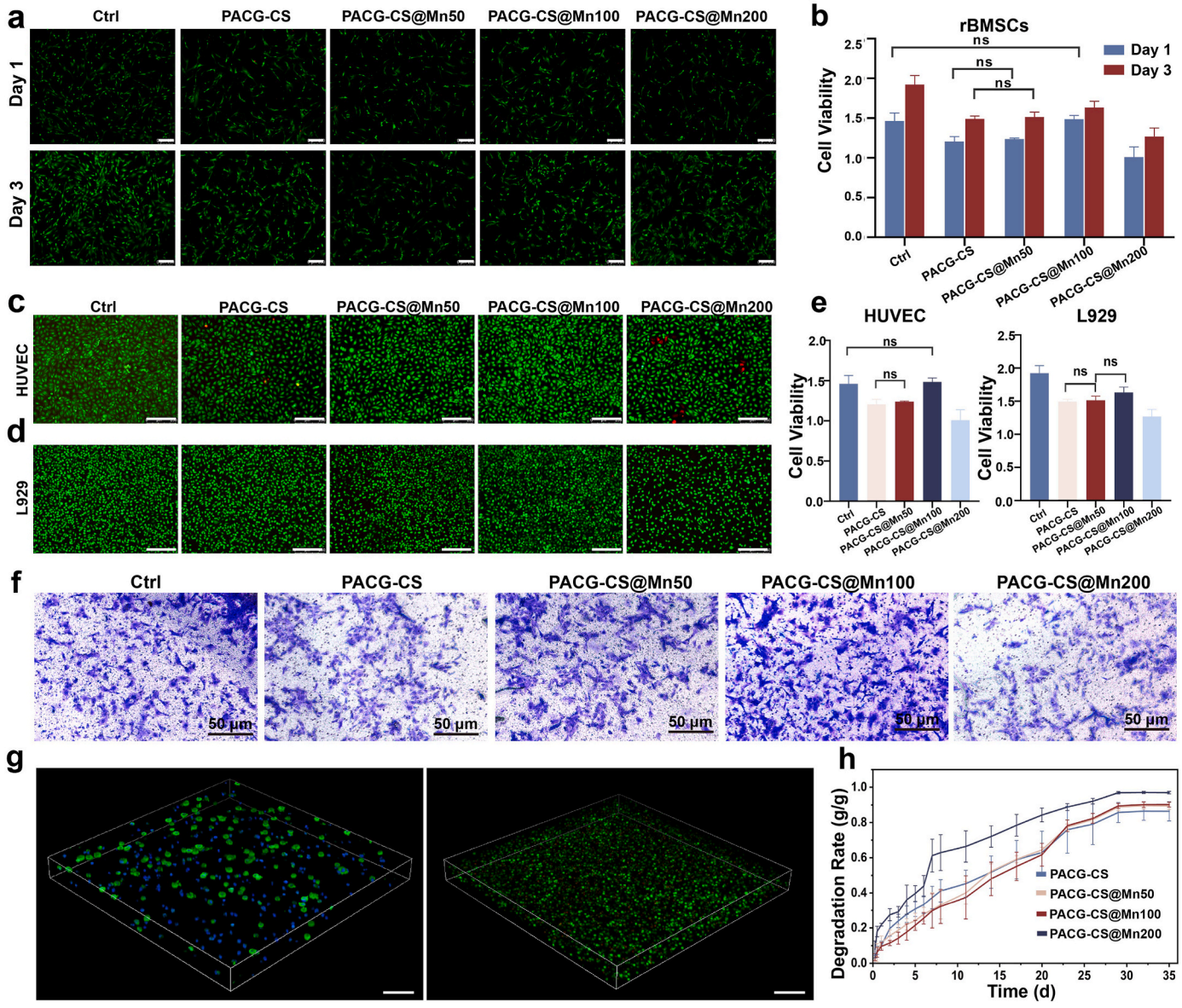

Fig. 2. ***In vitro*** **biocompatibility and cell migration abilities.** (a) Live-dead staining of control and various hydrogels co-cultured with BMSCs on day 1 and 3. Scale bars, 250 μm. (b) Assay of proliferative activity of both groups of cells (n = 3). (c, d) Live-dead staining using HUVEC and L929 cells co-cultured with each group of hydrogels. Scale bars, 250 μm. (e) Cell proliferation viability assay of HUVEC and L929 co-cultured with hydrogels (n = 3). (f) Cell migration assay of hydrogel co-culture by crystal violet staining. (g) Determination of cell recruitment capacity of PACG-CS@Mn100 DN hydrogel in cell migration assay. Left panel: cytoskeletal staining of macrophages within hydrogels; Right panel: live-dead staining of macrophages within the hydrogels. Scale bars, 250 μm. (h) *In vitro* degradation of PACG-CS composite hydrogel and various PACG-CS@Mn(III) DN hydrogels.

group [49,50]. Despite evidence that trivalent manganese used in this study exhibited cytotoxic characteristics similar to divalent manganese [51], it remains critical to control the manganese concentration to achieve an optimal balance between toxicity and bioactivity. Similarly, the crystal violet staining also revealed the highest pro-migratory activity of PACG-CS@Mn100 group in cell migration assay with hydrogel co-culture than the other two groups (Fig. 2f). Consequently, the PACG-CS@Mn100 group was selected as the experimental group for subsequent studies.

To verify cell distribution within the hydrogel and its regulation of inflammation-associated cell activity, the PACG-CS@Mn100 hydrogel was co-cultured with mouse macrophages (RAW264.7). Phalloidin staining was used to observe macrophage adhesion morphology, and live-dead staining assessed their biocompatibility (Fig. 2g). The results indicated that the regular anisotropic pores enabled the hydrogel with uniform distribution of macrophages and beneficial adhesion properties. Besides, the PACG-CS@Mn100 hydrogel was gradually degraded over 35 days *in vitro* due to its network skeleton constructed by strong non-covalent bonds (Fig. 2h), which could meet the appropriate degradation time for the implanted scaffolds in bone repair and regeneration. It was mentioned that similar degradation time of composite hydrogel and DN hydrogels not only reflected the dense network structure and high mechanical strength of the PACG-CS hydrogel, but also indicated the low Mn(III) concentration in the PACG-CS@Mn(III) hydrogel scaffold for ensuring *in vivo* safety. Accordingly, these above findings supported the excellent biocompatibility, effective recruitment and adhesion of immune cells and satisfactory biodegradability of the PACG-CS@Mn(III) hydrogels.

2.3. Fabrication of sandwich-layered hydrogel scaffolds

Taking the merit of this soaking strategy to tailor the network structure and mechanical performance, a sandwich-layered hydrogel was necessarily required and accessible to mimetic the multilayered

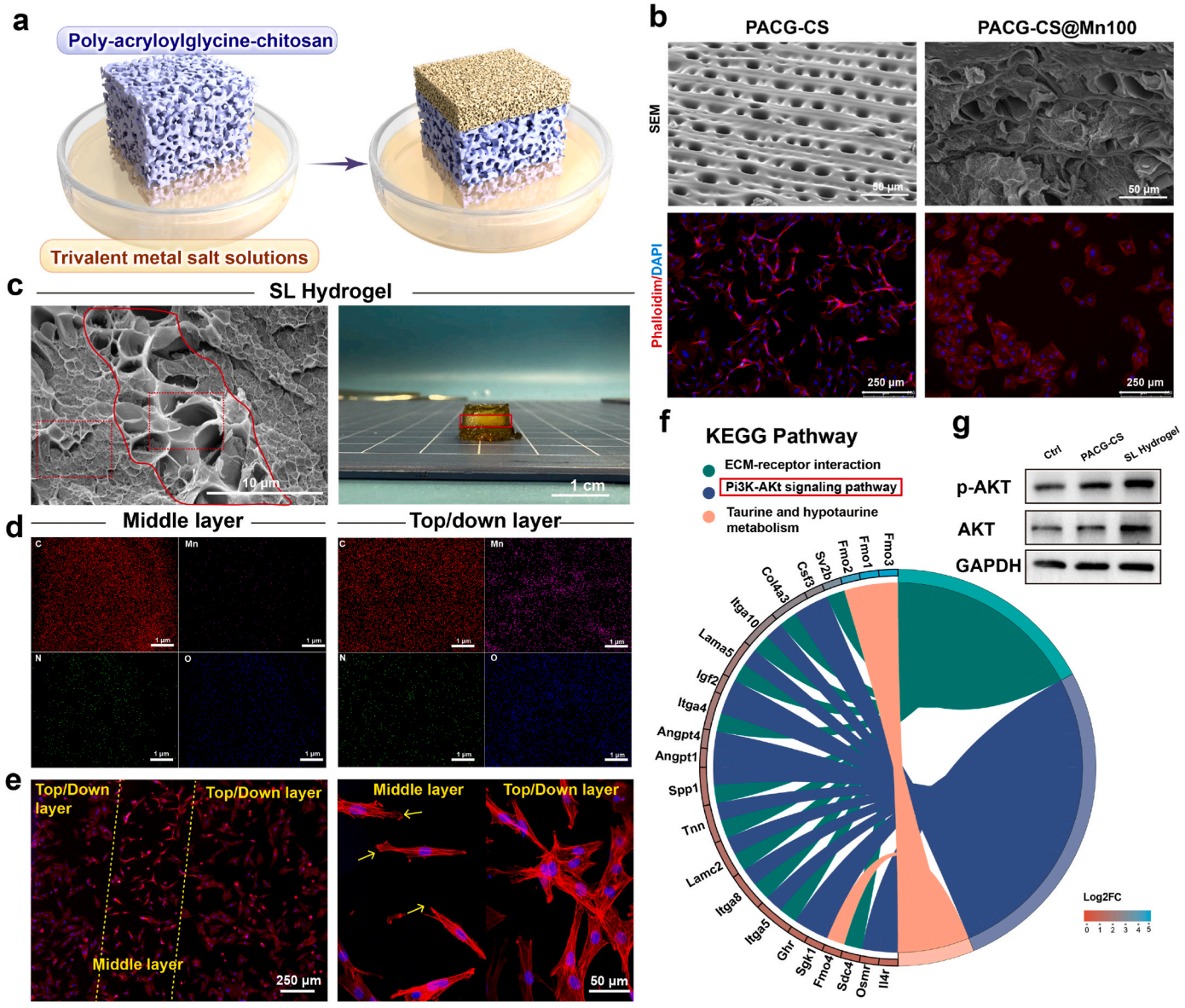

Fig. 3. Microscopic and macroscopic presentation of the cortical-cancellous simulated structure and morphological changes of BMSCs on the SL hydrogel. (a) Schematic preparation process of the SL hydrogels by an end-tail immersion method. (b) SEM images of PACG-CS and PACG-CS@100 hydrogels, and the morphologies of BMSCs on these hydrogels. (c) Microscopic and macroscopic observation of SL hydrogels. (d) EDS analysis of the interface structure of the middle and top/down layer of SL hydrogel. (e) Morphology of BMSCs on SL hydrogels. (f) KEGG pathway enrichment analysis of gene differences closely related to PI3K-AKT Pathway. (g) Western blotting detection of AKT and p-AKT protein level after co-culture of BMSCs with hydrogels.

cortical-cancellous structures of bone tissues. So, we used a simple end-tail soaking method to fabricate the SL hydrogel after immersing the PACG-CS hydrogel into 100 mM of manganese acetate solution at upper and lower surfaces for 1 h each. During the soaking process, we utilized a volume control method to regulate the thickness of SL hydrogels. Based on our previous works, under a fixed immersion depth, the penetration depth of metal ion solutions into the CS-based hydrogels were mainly determined by the ion concentrations and soaking time [35,47], but high concentration of salt solutions and prolonged soaking time could inevitably induce the ion diffusion throughout the hydrogels and failed the precise thickness. However, since the concentration of manganese ions was much lower than the concentration of carboxyl groups in PACG, the thickness of each hydrogel layer could be feasibly and precisely controlled by immersion depth and soaking time (Fig. 3a and Fig. S5). Compared to the unsoaked PACG-CS and PACG-CS@Mn100 DN hydrogels (Fig. 3b), by controlling the time and depth of the immersion solutions, SL hydrogel scaffolds with sandwich-layered hierarchical structures were produced both at micro and macroscopic levels while retaining their original morphologies at each layer (Fig. 3c). It was mentioned that compared with the traditional 3D printing and direct adhesion for construction of multi-layered hydrogel scaffolds, this end-tail soaking strategy offered the advantages of maintaining the integrity of layered structures while ensuring the seamless integration of multilayered hydrogel scaffolds. To verify the layer integration strength and homogeneity across the SL hydrogels, cyclic compression test was performed to evaluate the fatigue resistance under repeated loading. Fig. S6 showed that these SL hydrogels with various manganese immersion concentrations could maintain significant mechanical integrity and stability after 50 cycles at 30 % strain, indicating their elasticity and resilience for engineering scaffolds in a physiological setting.

EDS assay showed the formation of sandwich structure was obviously related to the distribution of manganese ions (Fig. 3d). Due to the difference in internal pore size between PACG-CS hydrogels and DN hydrogels, cells exhibited different adhesion patterns in the two types of hydrogels (Fig. 3b and Fig. S7). Meanwhile, the cell distribution on the cross-section of the SL hydrogel also reveals differences in internal pore sizes (Fig. 3e). Previous studies had shown that extracellular matrix stiffness could influence cell function by regulating the assembly and disassembly of the actin cytoskeleton. In mesenchymal stem cells, higher matrix stiffness often induced osteoblasts with a larger spreading area and higher levels of actin polymerization, while undifferentiated cells typically exhibited an elongated and spindle-shaped morphology [52]. In this study, BMSCs exhibited a slenderer morphology in the middle layer (PACG-CS composite hydrogel) while a more uniform and unfolded shape was displayed in the top and down layers (PACG-CS@Mn100 DN hydrogel), which was attributed to that the stiff layer could enhance osteogenic differentiation by increasing the cell spreading area compared to the soft layer, and thus further revealing the significant influence of geometrical difference on BMSC adhesion.

To further investigate the role of sandwich-layered microstructure on osteogenic gene expression in BMSCs, we performed RNA-seq analysis on SL hydrogel and blank control. Based on the quantitative expression results, differential gene analysis was conducted to identify the differentially expressed genes between the two groups (Fig. S8). Kyoto encyclopedia of genes and genomes (KEGG) analyses revealed an association between the identified set of genes and the phosphatidylinositol 3-kinase (PI3K)-protein kinase B (AKT) pathway (Fig. 3f). Among these, integrin-related genes significantly associated with the interactions between the cells and ECM, such as ITGA5, ITGA8, and ITGA10, are notably upregulated. Some researchers have pointed out that integrin α5, encoded by ITGA5, acts as a 'bridge' for the mechanical cues between cells and the matrix, further promoting the osteogenic differentiation of pre-osteoblasts by sensing high matrix stiffness [53]. In this study, stem cells activated integrin-related genes by perceiving the strong matrix stiffness of SL hydrogels, subsequently activating osteogenic-related genes such as spp1 through the PI3K-AKT pathway. Similarly, Western blot analysis of SL hydrogels co-cultured with BMSCs confirmed a significant upregulation of AKT and p-AKT in the SL hydrogel group (Fig. 3g), which was consistent with the promotion of spatial topography on osteogenic differentiation of stem cells as demonstrated in many recent studies [54,55].

2.4. *In vitro* protective efficacy against oxidative stress

It is well known that divalent manganese ions can act against oxidative stress both inside and outside cells [50,56], and many studies have also focused on the use of trivalent manganese to mimic manganese-based superoxide dismutase (MnSOD) [41,43,57]. Thus, we employed cyclic voltammetry to verify whether the manganese in the SL hydrogel exhibits redox reactions similar to those of MnSOD and catalase (Fig. S9). Before that, we firstly measured the manganese ion release behaviors at 12 h, 24 h, 48 h, 72 h, and 96 h using inductively coupled plasma mass spectrometry (ICP-MS) technology (Fig. S10). In the normal environments, manganese ions could be slowly released and exuded from the SL hydrogels through the free diffusion, and maintain a certain concentration over a longer duration (a cumulative release of 50 % at 96 h), which further revealed the strong carboxyl/Mn(III) chelation within the network. Once exposure onto the oxidative stress conditions, the manganese ions could be rapidly released within 24 h to exert the antioxidant activity via MnSOD-like effects due to the shift of equilibrium reaction, thus regulating the oxidative stress environments, especially in the early stage of fracture healing. Furthermore, as shown in Fig. 4a, the SL hydrogel displayed a positive oxidation peak and a negative reduction peak, and the ratio of oxidation peak to reduction peak was slightly greater than one, which indicated its stronger oxidizing ability than reducing ability, similar to the results of manganese porphyrin mimics *in vitro* [58]. In order to further validate the peroxidase-like activity, hydrogen peroxide (H_2O_2) scavenging experiment was conducted in Fig. 4b and Fig. S11a. The SL hydrogels soaked in different manganese concentrations exhibited stepwise clearance activity of H_2O_2, indicating its peroxidase-like reaction.

Cellular senescence induced by reactive oxygen species (ROS) inhibited the osteogenic microenvironment [59], while biomaterials containing antioxidants could reduce ROS accumulation and promote bone regeneration by mimicking the activity of antioxidant enzymes [60]. By this token, SL hydrogels was capable to possess protective efficacy on cell activity and tissue regeneration under an oxidative stress microenvironment. To simulate high oxidative stress environment following fracture injury, we firstly attempted to establish a hyperactive ROS environment *in vitro* by adding H_2O_2 to mimic the inflammatory condition and evaluate the protective effect of SL hydrogel on the BMSCs. As a key protein mediating cellular oxidative stress injury, intracellular p53 protein was significantly upregulated after H_2O_2 treatment (Fig. 4c), implying the cellular damage and apoptosis by oxidative stress [61]. On the contrary, addition of the manganese-containing SL hydrogel led to a downregulation of p53 protein expression, thus demonstrating the specific activation of MnSOD and protective effect of SL hydrogel against the cellular oxidative stress-related injury. Therefore, along with the slow release of exogenous supplementation of trivalent manganese, the expression of MnSOD could maintain high level in cells and exert sustain promotion effect for more than two weeks (Fig. 4d and e), indicative of the long-lasting cellular resistance to oxidative stress of SL hydrogel scaffold.

Additionally, β-galactosidase staining also testified that the SL hydrogel had a protective effect against the increased oxidative stress-related DNA damage caused by H_2O_2 treatment (Figs. S11b and c). Subsequently, we also investigated ability of its anti-oxidative stress on eliminating the endogenous ROS (i.e., superoxide anion) by treating the macrophages with LPS. ROS-specific fluorescent probe staining revealed the efficient inhibition of upregulation process of ROS in macrophages (Fig. 4f and Fig. S12). Therefore, it could be speculated that the slow release of manganese trivalent ions could counteract the local oxidative

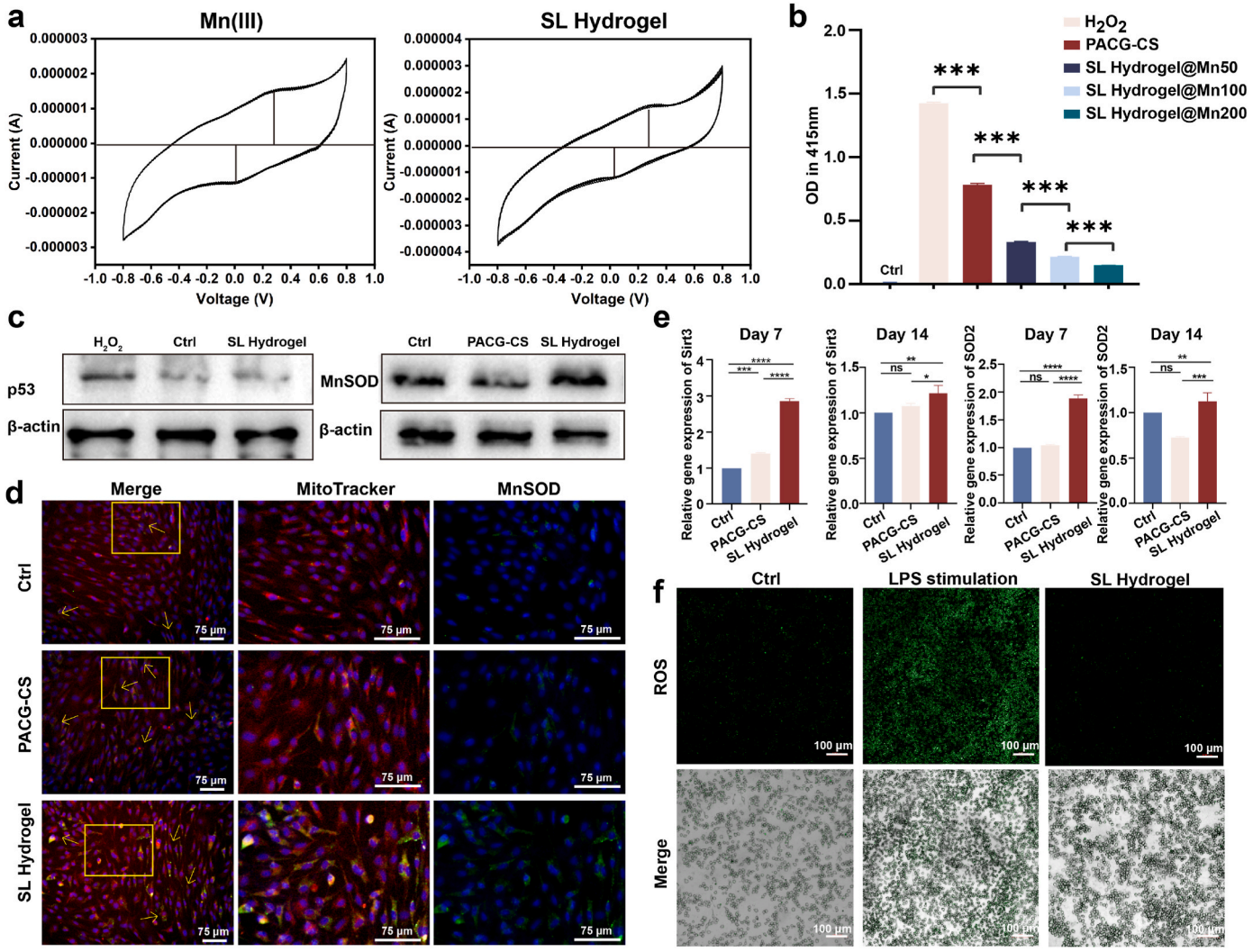

Fig. 4. *In vitro* protective efficacy of the SL hydrogel on BMSCs under oxidative stress microenvironments. (a) Comparison of redox curves of manganese acetate and SL hydrogel after three redox cycles. (b) *In vitro* H_2O_2 clearance activity by SL hydrogel treatment (n = 3). (c) p53 and MnSOD western-blotting on BMSCs after H_2O_2 and SL hydrogel treatments. (d) Immunofluorescence analysis of MnSOD colocalized with mitochondria. (e) qPCR assays of MnSOD and Sirt3 after co-culture for 7 and 14 days (n = 3). (f) ROS-specific fluorescent probe assay for LPS-stimulated macrophages and SL hydrogel treatment.

stress microenvironment via the direct scavenging of hyperactive superoxide anions and H_2O_2 and activating superoxide dismutase *in vivo* to prevent the cell damage. These findings implied that the SL hydrogel could effectively resist the both endogenous and exogenous oxidative stress by specific upregulation of MnSOD and durably exert the protective efficacy on cells under oxidative stress microenvironments.

2.5. *In vitro* osteogenesis activity

The *in vitro* osteogenic ability of biomimetic SL hydrogels was evaluated through osteogenic-specific staining and angiogenesis assays (Fig. 5a). Alkaline phosphatase (ALP) staining and alizarin red S (ARS) staining results demonstrated that the hydrogel significantly enhanced osteogenic tendency of *in vitro* BMSCs after osteogenic induction both at 7 and 14 days. ALP quantification and staining indicated a significant enhancement in ALP activity at all stages of osteogenic induction. ARS suggested the presence of significant osteocalcin nodules in the culture medium after 2 weeks of co-cultivation, indicating that the sandwich-layered hydrogel possessed remarkable osteogenic induction activity *in vitro*, which ascribed to its excellent biocompatibility and effective anti-oxidative stress ability. Similarly, the osteogenesis-related specific proteins (COL1a1, Runx2 and BMP4) were upregulated in both PACG-CS and SL hydrogel groups (Fig. 5b). qPCR assays of early osteogenic genes (spp1, sp7, Runx2 and ALP) and mid-late genes (COL1a1 and BGLAP) also demonstrated SL hydrogel's efficacy in promoting osteogenesis (Fig. 5c). To further visualize the osteogenic effects *in vitro*, we performed the immunofluorescence staining of intracellular Runx2 proteins, which suggested that the SL hydrogels could significantly promote upregulation of Runx2 osteogenesis-related proteins (Fig. 5d). Additionally, *in vitro* angiogenesis assays using human umbilical vein endothelial cells (HUVEC) treated with SL hydrogels demonstrated significant angiogenic activity. Relevant proteins, such as VEGFA, were also found to be significantly upregulated in the hydrogel treatment group. The release of manganese ions from SL hydrogels promoted the angiogenesis, further supporting the crucial role in enhancing osteogenic process (Fig. S13).

2.6. *In vivo* bone repair efficiency of SL hydrogels with restrictive pro-angiogenesis

To further evaluate the osteogenic properties of the hydrogels, PACG-CS and SL hydrogel scaffolds were implanted into the 5-mm size of rat skull defects (Fig. 6a). SEM images showed each layer thickness of SL hydrogels with 200 μm, 600 μm and 200 μm to biomimetic the

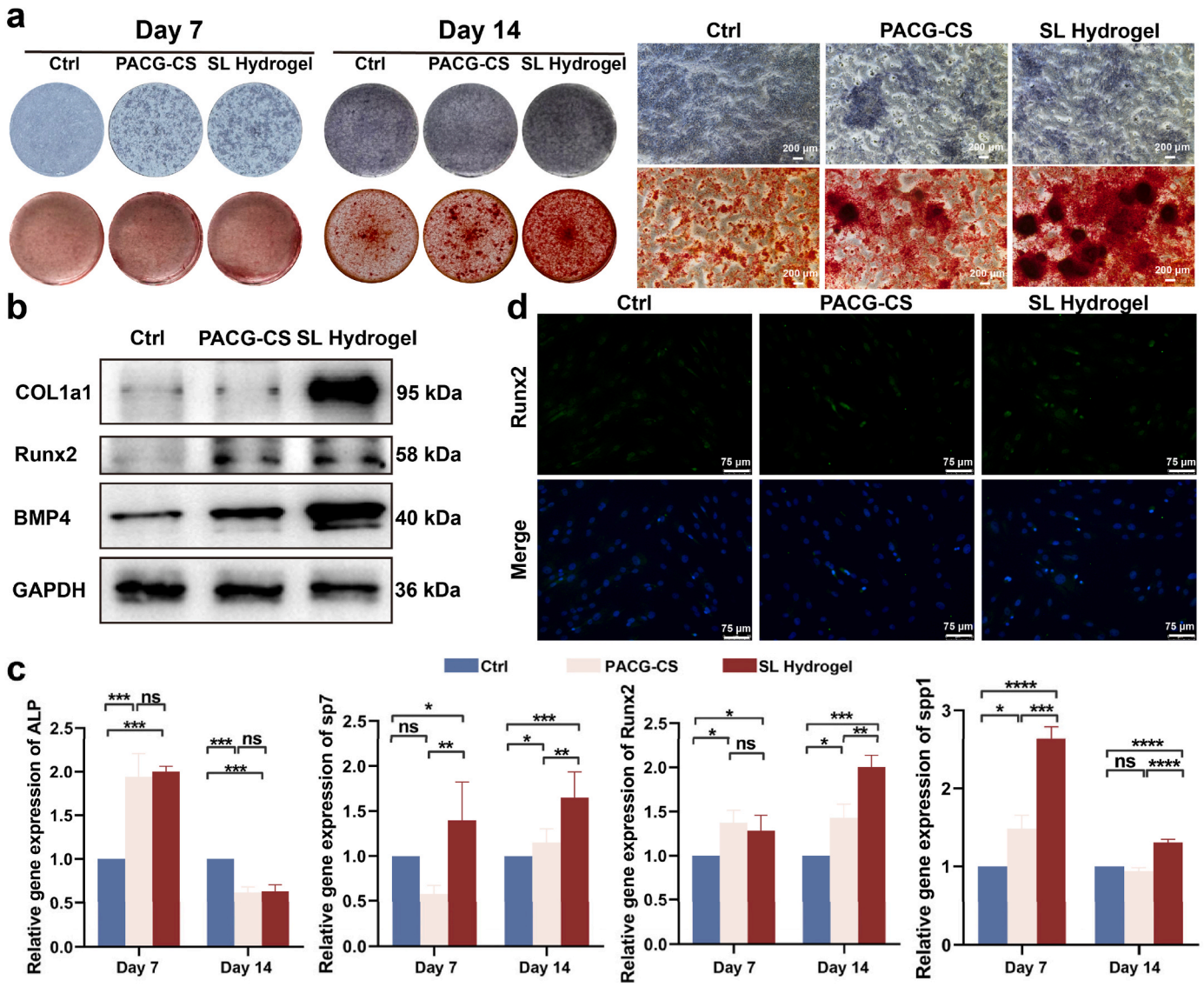

Fig. 5. ***In vitro*** **osteogenic performance.** (a) ALP staining and ARS staining of various hydrogels on days 7 and 14 after osteogenic induction. (b) Western-blotting of osteogenic-specific proteins. (c) qPCR quantification of early and mid-late osteogenic-specific RNAs (n = 3). (d) Immunofluorescence staining of Runx2 protein colocalized with the nucleus.

multilayered cortical-cancellous structure of bone tissues. Energy-dispersive X-ray spectroscopy (EDS) indicated that the distribution of manganese ions in the top and down layers of SL hydrogel (Fig. 6b). After *in-vivo* implantation for 6 and 12 weeks, Micro-CT showed the visible bone island formation in both hydrogel groups at 6 weeks, with denser bone islands in the SL hydrogel group. At 12 weeks, nearly complete repair was observed in the SL hydrogel group compared to the partial osteogenesis in the PACG-CS group and little osteogenesis at the defect edges in the control group (Fig. 6c). Quantitative results further demonstrated the repair efficacy of these three groups (Fig. 6d). The trabecular number (Tb.N) and bone volume fraction (BV/TV) showed significant differences in the early and middle stages of the process, and the stratified biomimetic SL hydrogel presented best performance. Trabecular thickness (Tb.Th) did not show significant changes across all groups during the early and middle stages of osteogenesis, indicating that this kind of biocompatible hydrogels supported normal osteogenesis at the microscopic level. The degree of anisotropy (DA) is commonly used to evaluate the orientation and symmetry of trabeculae, with a higher value indicating greater anisotropy [62]. In this study, differences in bone anisotropy were observed between weeks 6 and 12. At week 6, PACG-CS group exhibited significantly higher DA due to the regular 'transverse-longitudinal' interlacing structure. By week 12, SL hydrogel group showed the increasing DA in the middle and late stages of osteogenesis. This improvement may be due to the biomimetic sandwich-layered structure of SL hydrogel group that provided a good framework and splendid microenvironment regulation for the full-thickness osteogenesis. It was well-established that blood vessels were distributed throughout full-thickness bone tissue and played a supportive role in bone regeneration. However, within the cortical and trabecular bone, there were differences in vascular distribution [63].

Numerous studies have shown that angiogenesis could significantly promote the bone regeneration [64]; however, it could only support bone formation without creating an effective layered structure of cortical and trabecular bone. In bone anatomy, blood vessels in cortical bone were relatively sparse and arranged in an orderly manner while the vascular network in trabecular bone was more abundant and complex. We proposed that this difference in vascular microstructure may contribute to varying regeneration outcomes. Therefore, the stratified biomimetic SL hydrogel should have the function of limited vascular regeneration. While SL hydrogels had significant pro-angiogenic effects,

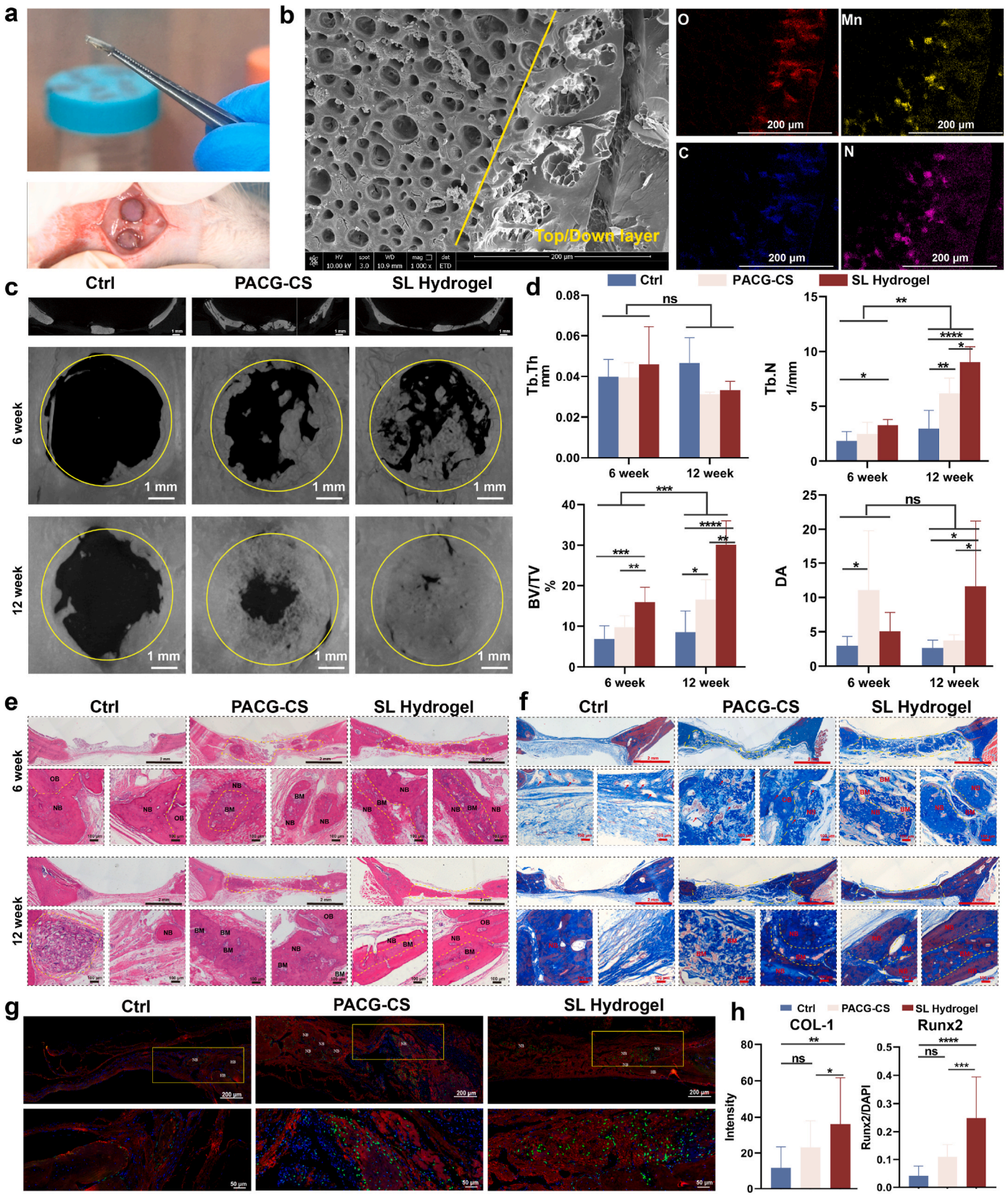

Fig. 6. *In vivo* bone regeneration. (a) *In-vivo* implantation of hydrogel scaffolds into rat cranial defects. (b) SEM images and EDS analysis of the implanted SL hydrogels for the repair of cranial defects in rats. (c, d) Micro-CT evaluation of the repair effect and their quantitative data in different samples (n = 4). (e) H&E staining of cranial tissue specimens at 6 and 12 weeks. NB means new bone, and BM means bone marrow. (f) Masson trichrome staining of rat cranial samples at 6 and 12 weeks. (g) Immunofluorescence evaluation of bone repair in tissue sections. Runx2: green color, DAPI: blue color, and COL-I: red color. (h) Quantitative analysis from image-J of fluorescence data from multiple samples (n = 4).

layered scaffolds with various apertures could restrict angiogenic areas to better fit physiological structures *in vivo*. Compared to the non-layered PACG-CS group, the layered SL hydrogel group demonstrated the superior performance in the regional formation of bone marrow on the basis of immunofluorescence, H&E and Masson staining results (Fig. 6e, f and Fig. S14). In the bone regeneration region, bone marrow was distributed between the newly formed bone in the SL hydrogel group, allowing for the limited vascular regeneration by week 12, which facilitated the structural restoration of the bone. In contrast, bone formation in the PACG-CS group was limited due to insufficient mechanical support and unrestricted vascular regeneration, which hindered the formation of dense cortical bone and severely impacted the mechanical properties of newly formed bone (Fig. 6e, f). Similarly, from a macroscopic perspective, histological analysis and micro-CT imaging (Fig. 6c) of osteoblast samples during the mid to late stages revealed fractures and deformations in the osteoblast layer of the non-layered PACG-CS scaffold. In contrast, the layered structure of SL hydrogel effectively supported the orderly regeneration of bone and facilitated local osteogenesis.

Immunofluorescence staining of rat skull samples further demonstrated the superior osteogenic effect of the stratified biomimetic SL hydrogel (Fig. 6g and h). Runx2 expression was significantly

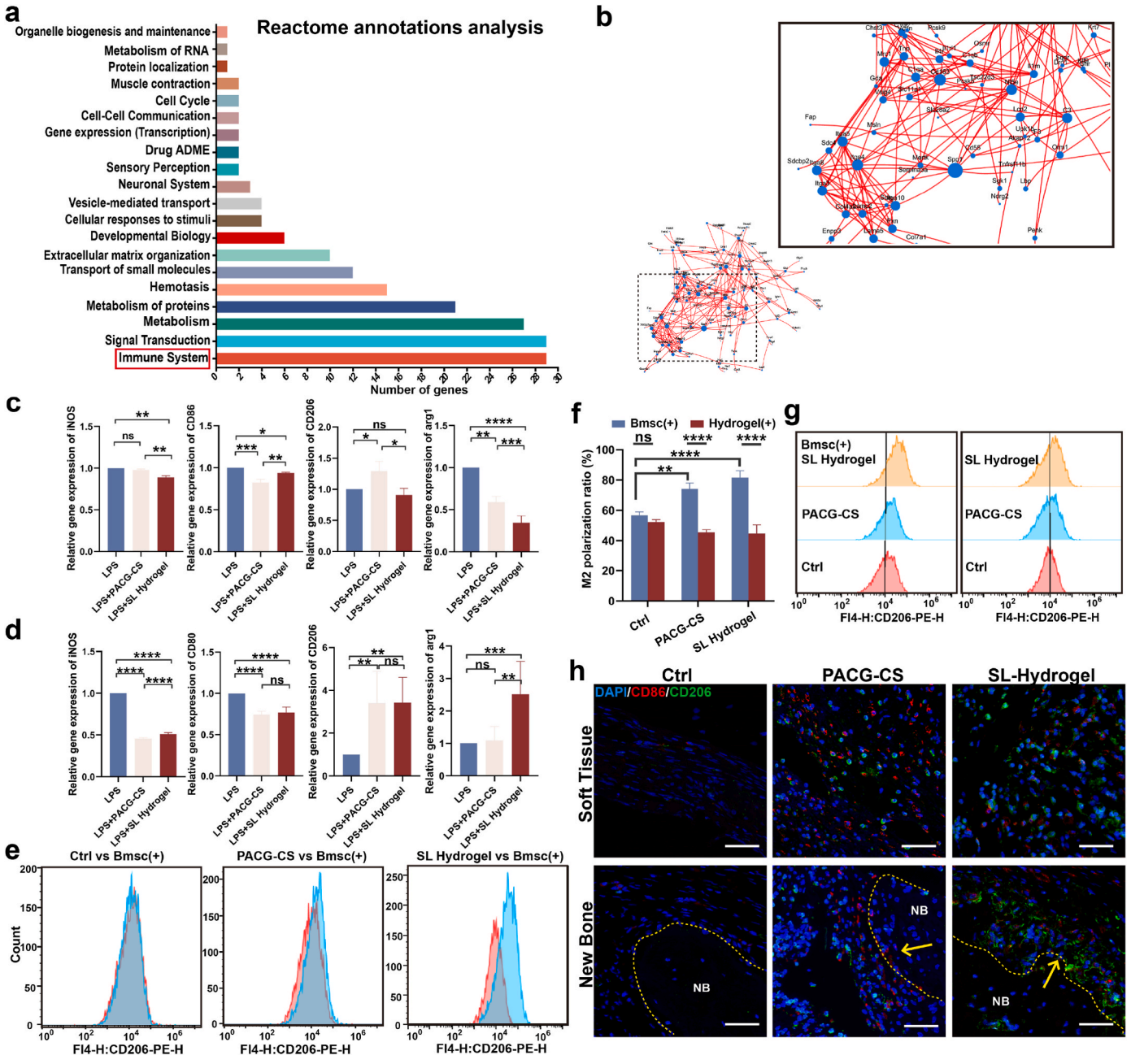

Fig. 7. Effects of osteoblasts on immune regulation. (a) Reactome annotation analysis of the close relation between differential genes and immune activation. (b) Analysis of PPI networks after co-culture of hydrogel and mesenchymal stem cells. (c) Expression of macrophage polarization-related genes detected by qPCR after hydrogel co-culture with macrophages (n = 3). (d) Macrophage polarization phenotype of macrophages co-cultured with hydrogel-pretreated BMSCs detected by qPCR (n = 3). (e) Detection of macrophage M2 type polarization in co-culture groups by flow cytometry. Wherein, bmsc(+) means multicellular co-culture. (f) Polarization quantification by flow cytometry of macrophages (n = 3). (g) Differential ratio of polarization of macrophages after direct versus indirect co-culture in hydrogels detected by flow cytometry. (h) Immunofluorescence staining of macrophage polarization states in animal sections (Blue: DAPI; Red:CD86; Green:CD206. Scale bar, 50 μm). The arrow indicates the interface between newly formed bone and macrophages.

upregulated in the SL hydrogel group, and microenvironmental regulation of extracellular matrix in the hydrogels also led to a significant increase in COL-I expression. Similarly, immunohistochemical staining also revealed specific expression of osteogenesis-related proteins, including OCN and Runx2, as well as COL-I production (Fig. S15). Further analysis of the fluorescence distribution of COL-I revealed the formation of an alternating collagen fiber arrangement similar to that of normal bone tissue in the SL hydrogel group, whereas such structures were not obvious in the non-layered PACG-CS group (Fig. S16). This may also be related to the staged degradation during osteogenesis in the biomimetic sandwich-layered scaffolds.

2.7. Mechanism of immune regulation centered on osteoblast activation

To further explore the functional roles of the hydrogel beyond directly promoting osteogenesis, we conducted an in-depth analysis of the transcriptomic data. Reactome annotation analysis showed a significant upregulation of immune-related pathways, indicating an association with immune cell activation in BMSCs (Fig. 7a). The protein-protein interaction (PPI) network also supported this finding, showing significant interactions between the key gene spp1 involved in bone regeneration and various integrin receptor-encoding genes, such as ITGA8 (Fig. 7b). In combination with the above mentioned direct osteogenic effects, these findings suggested that the layered structures of biomimetic hydrogels may regulate osteogenic differentiation of stem cells through integrin receptor-mediated activation of the PI3K-AKT pathway.

There is increasing evidence that biomaterials can influence osteoclasts and osteoblasts by modulating myeloid cells such as macrophages, thereby regulating bone remodeling and supporting bone regeneration [65]. In addition, BMSCs can regulate immune cell polarization, especially macrophage polarization, through a variety of mechanisms, including exosome release and paracrine signaling [66]. However, the conversion of stem cells into osteoblasts and the change of local immune microenvironment during the healing of bone defect represent a complex process. So, we co-cultured hydrogel-pretreated BMSCs with IFN-γ/LPS-pretreated macrophages for 24 h and examined the macrophage polarization phenotype using qPCR and flow cytometry. The results indicated that M1 phenotype of pretreated macrophages was significantly upregulated (Fig. S17). Macrophages co-cultured with the hydrogel directly did not show significant phenotypic changes (Fig. 7c), whereas macrophages co-cultured with hydrogel-pretreated BMSCs exhibited a downregulation of the M1 phenotype and an upregulation of the M2 phenotype (Fig. 7d). This was further evidenced by the percentage of CD206 and CD80 positive cells in flow cytometry analysis (Fig. 7e and Fig. S18). These findings demonstrated that the unique stratified biomimetic structure of hydrogel influenced the macrophage polarization by specifically activating the immunostimulatory effects of BMSCs, resulting in a shift of macrophage from a pro-inflammatory to an anti-inflammatory phenotype.

To further confirm whether the macrophage phenotypic shift was directly induced by the hydrogel or mediated by BMSCs, we performed a flow cytometry comparison of CD206-positive cells between LPS-induced macrophages directly treated with hydrogel and those in the co-culture group described above. The results showed that polarization of macrophage M2 in the direct treatment group was significantly lower than that in the co-culture group (Fig. 7f), and there was no significant difference in the M2 cell polarization rate in the direct treatment group (Fig. 7g). In addition, to confirm osteoblast-based immune microenvironmental regulation, we performed macrophage subtype immunofluorescence staining on 6-week cranial bone sections (Fig. 7h). The results showed that in soft tissue, the hydrogel-treated group exhibited activation of the immune environment, but no predominant macrophage population was observed. In contrast, there were a large number of significantly activated M2 macrophages around new bone in the SL hydrogel-treated group, indicating that osteoblasts induced by SL hydrogel could also exert a unique immune microenvironment regulatory effect. Consequently, the SL hydrogel induced osteoblast differentiation through its unique spatial topology, subsequently modulating the immune microenvironment, which was in line with the theoretical framework of osteoblast regulation of immune responses [67–69]. However, fracture healing was a dynamic process involving multiple cell types, where the osteogenesis required the close cooperation of osteoblast and pro-repair phenotypes of macrophages. Therefore, understanding the relevant mechanisms to promote fracture healing from the perspective of multicellular communication represents a promising research direction.

To further explore potential pathways, single-cell data analysis was conducted using the SCP1337 public dataset [70], which included both *in vivo* derived and *in vitro* cultured osteoblasts. We identified a specific spp1 high-expression subpopulation present in the *in vivo* environment (Fig. S19a). Additionally, we performed a CellChat® analysis to explore the relationship between this subpopulation and various macrophage groups. The results indicated that the spp1-CD44 pathway was most likely to mediate this process (Figs. S19b and c). Meanwhile, this also indirectly validated that SL hydrogel possessed remarkably biomimetic microstructures to promote mesenchymal stem cell-like *in vivo* osteogenic differentiation. Although the specific mechanism by which osteoblasts promote macrophage polarization has not yet been clarified, spp1 may be a key protein linking this osteogenic immune-related effect. Further studies are needed to investigate the mechanism underlying this interaction.

3. Conclusion

In summary, we developed a biomimetic SL hydrogel featuring sandwich-layered structures using a stepwise end-tail soaking strategy for robust full-thickness repair of bone defects. Taking advantage of multiple physical interactions and carboxyl/Mn(III) complexation, SL hydrogel showed flexible structural fabrication, biomimetic hierarchical network, excellent mechanical performance, favorable biocompatibility and excellent radical scavenging efficiency, thus benefiting for BMSCs activity, proliferation and osteogenic differentiation. By control of the manganese ion valent and concentration through a peroxidase-like reaction, SL hydrogel was endowed with enhanced MnSOD activity, remarkable radical scavenging capacity and protective efficacy on cells within oxidative stress microenvironments. Under this circumstance, *in vivo* results indicated that the structural differences and manganese distribution across various regions of SL hydrogels exhibited restrictive angiogenesis mechanism, effectively simulating the vascular distribution within cortical and trabecular bone. More importantly, the mechanical cues inherent of stratified structure mediated macrophage phenotype transitions that was consistent with the stem cell-osteoblast differentiation process via the PI3K-AKT pathway, ultimately achieving full-thickness bone regeneration with optimal healing quality. Given the widespread presence of metal coordination effects using this divisional soaking strategy, we are convinced that the proposed approach is universal and applicable for producing more bioactive metal-based hierarchical or gradient porous scaffolds with expandable functionalities for complex anisotropic tissue regeneration. Moreover, the concept of immune regulation centered on osteoblast activation also holds broad practical applicability and can significantly improve the theoretical understanding of immune microenvironment changes during bone repair.

4. Materials and methods

4.1. Materials

Short-chain chitosan (degree of deacetylation>90 %, viscosity 45 mPa s for 1 % (w/v) solution, molecular weight: ≈10 kPa, Jinhu Company), glycine (Tokyo Chemical Industry Co., Ltd.), acryloyl chloride

(Energy Chemical Reagent Co., Ltd.). Sodium hydroxide (NaOH), hydrochloric acid (HCl), sodium chloride (NaCl) and calcium chloride ($CaCl_2$) (Sinopharm Chemical Reagent Co., Ltd.). Manganese (III) acetate dihydrate (J&K Scientific Co., Ltd.), N, N′-methylene-bis-acrylamide (MBA) and 2-hydroxy-4'-(2-hydroxyethoxy)-2-methylpropiopheno (Irgacure 2959) (Alfa Aesar Co., Ltd.), ethyl acetate and petroleum ether were obtained from Concord Reagent Co., Ltd. and used directly.

4.2. Synthesis of ACG monomer

Typically, 4.5 g of glycine (60 mmol) was dissolved in 60 mL of a solution of potassium hydroxide (2 M). The mixture was cooled at 0 °C with ice water bath for 10 min. In brief, 6 mL of acryloyl chloride (73.6 mmol) was added dropwise to the mixture using a dropping funnel. After stirring for at room temperature for 3 h, the solution was washed with diethyl ether for two times and the aqueous phase was then acidified to the pH 2.0. The product was extracted with ethyl acetate for three times. After drying the organic phase over $MgSO_4$, the residue was concentrated with a rotary evaporator to obtain white solids with a yield of 74 %.

4.3. Preparation of PACG-CS composite hydrogel and PACG-CS@Mn (III) DN hydrogel

PACG-CS composite hydrogel was prepared by photoinitiated radical polymerization. Briefly, ACG (0.6 g), CS (0.075 g) and Irgacure 2959 (0.01 g, 1 mol% of ACG monomer) were dissolved in deionized water (4 mL) and further radiated under UV radiation (150 W) for 4 h to obtain the PACG-CS composite hydrogel. Subsequently, PACG-CS composite hydrogels were soaked in different manganese acetate solutions (50, 100 and 200 mM) for 1 h to prepare PACG-CS@Mn(III) DN hydrogels.

4.4. Preparation of SL hydrogel

100 mM of manganese acetate solution was dropped on a hydrophobic plastic plate to control the thickness of the liquid surface, and the PACG-CS composite hydrogel was taken to soak the upper and lower surfaces for 1 h to prepare SL hydrogel. Control of the liquid volume in a fixed container (6 cm cell culture dish) can conveniently determinate the liquid surface height.

4.5. Characterizations

^{1}H NMR spectrum was measured on a Bruker Avance 400 or Bruker Avance III 400 HD NMR spectrometer using D_2O as solvent. Fourier transform infrared spectroscopy (FTIR) was taken on a TENSOR-27 spectrometer. Scanning electron microscopy (SEM) images were acquired from a JSM-6700F microscope. X-ray photoelectron spectroscopy (XPS) curves were measured on a Thermofisher Nexsa. Rheological properties of the hydrogels were tested using a Thermo Fisher HAAKE MARS III rheometer equipped with parallel plate geometry (20 mm of diameter) at a gap of 1.0 mm. The hydrogel was measured at 25 °C in a frequency range of 0.1–10 rad s^{-1} at a strain of 5 %. Nitrogen adsorption-desorption were measured on an asap2460. The mechanical testing was conducted on an electromechanical universal testing machine (C43.104Y, MTS, China).

4.6. Swelling and degradation ratios

The initial weight of freeze-dried hydrogel samples (W_0) was recorded. Then, samples were immersed in PBS at 37 °C, and the PBS was replaced every 2 days. In the swelling study, samples were weighed at the specified time and recorded as W_t. The swelling ratio (%) of the samples was calculated using following formula:

$$\text{Swelling Ratio } (\%) = (W_t - W_0) / W_0 \times 100\%$$

For the *in vitro* degradation, the hydrogel samples were rinsed, lyophilized, and weighed after 0 (W_0) and various specified days, and the weights were recorded as W_t. The degradation ratio (%) of the samples was calculated using the following formula:

$$\text{Degradation Ratio } (\%) = (W_0 - W_t) / W_0 \times 100\%$$

4.7. Cell culture

rBMSCs, HUVECs, Raw 264.7 and L929 cells were used in this work. rBMSCs and Raw 264.7 were cultured in DMEM medium with the supplement of 10 % FBS and 1 % P/S. HUVECs were cultured in ECM medium with 5 % FBS, 1 % ECGS/H, and 1 % P/S supplemented. The cells were cultured in RPMI 1640 medium supplemented with 10 % v/v FBS and 1 % P/S.

4.8. Cell adhesion, proliferation and differentiation

First, polyhedron-like scaffolds were sterilized for cell experiments. For the cell adhesion assay, cells were cultured for 1 day and fixed with 4 % paraformaldehyde (PFA). Alexa Fluor 647-conjugated phalloidin and DAPI were applied to stain the cytoskeleton and nuclei, respectively. Fluorescence images were observed by DMI8 (Leica, Germany). The proliferation activities of cells (rBMSCs, HUVECs, L929 and RAW264.7) were performed by CCK-8 assay (solarbio, China) [71]. Briefly, at each time point, CCK-8 working solution was added to the medium and incubated for 1.5 h. Subsequently, the absorbance of supernatant of the medium was measured at 450 nm.

4.9. Transwell migration assay

Cell migration was detected using Transwell chambers (Corning, USA). rBMSCs (2×10^4 cells/well) were seeded in the upper chamber, while a medium with various hydrogels was added to the bottom chamber for 24 h. Subsequently, the cells in the upper chamber were washed and fixed with 4 % paraformaldehyde for 20 min, followed by permeabilization with 0.1 % TritonX-100 for 30 min. Finally, the cells were stained with crystal violet solution (beyotime, China) and photographed and observed under a light microscope.

4.10. In vitro release behaviors

ICP-MS were measured on an Agilent 7700 (MS), and each group of Mn(III)-containing hydrogels were immersed in PBS solutions for 12 h, 24 h, 48 h, 72 h, and 96 h. After the soaking period, the hydrogels were removed, freeze-dried, and subjected to complete acid digestion. The manganese ion concentration in the digestion solution was then measured. The difference between the manganese ion concentration in the digestion solution at each time point and at 0 h represented the amount of manganese ions released during the corresponding time period. The *in vitro* oxidative stress environment was established using 100 μM hydrogen peroxide (H_2O_2), and the specific detection procedures were the same as described above.

4.11. ROS detection

Raw264.7 cells (5×10^4 cells/well) were seeded onto the surface of the hydrogel in a 24-well plate. In order to evaluate the intracellular ROS levels, the cells were labeled with the fluorescent DCFH-DA probe from the ROS assay kit.

4.12. Osteogenic differentiation

After being cultured for 7 and 14 days, the ALP activity of BMSCs was evaluated using a bicinchoninic acid (BCA) protein kit (Vazyme, China) and an ALP kit (beyotime, China). Besides, ALP staining was completed

by an ALP staining kit (beyotime, China). After 14 days of incubation, calcium nodules were stained with 1 % AR. After being dissolved in a 10 % cetylpyridine chloride solution, the calcium nodules were quantified by measuring the optical density value at 540 nm. Both AR and ALP staining of cells were observed via a stereomicroscope.

4.13. PCR assay

RT-qPCR was applied to measure the expression of specific genes as previously reported. The genes expression level was calculated by $2^{-\Delta\Delta Ct}$ method. The primer sequences were listed in Table S2.

4.14. Western blotting

Cells were treated with RIPA lysis buffer to extract total proteins for Western blot analysis. The protein concentration was determined using a BCA Kit (Vazyme, China). Equal amounts of protein were separated by 10–15 % SDS-PAGE and transferred onto a PVDF membrane. After washing the membranes with TBST and blocking them with 5 % skim milk for 1 h, they were incubated with primary antibodies overnight at 4 °C. PVDF membranes were then washed thrice with TBST and incubated with HRP-labeled secondary antibody at room temperature for 2 h. Chemiluminescent signals were developed using the enhanced chemiluminescent reagents and detected using the Tanon Imaging System (Tanon-4600).

4.15. Runx2 immunofluorescence staining assays

After BMSCs were cultured on different scaffolds for 48 h, the scaffolds were rinsed with PBS solution and fixed in 4 % paraformaldehyde. Then, Runx2 immunostaining was performed using rabbit polyclonal antibody (abcam No: ab192256) and Alexa Fluor 488.

4.16. MnSOD2 immunofluorescence staining assay

After BMSCs were cultured on different scaffolds for 48 h, the scaffolds were rinsed with PBS solution and fixed in 4 % paraformaldehyde. MnSOD2 immunostaining was performed using the rabbit polyclonal antibody (proteintech No: 24127-1-AP) and the Alexa Fluor 488.

4.17. Phalloidin staining

Cells were fixed with 4 % paraformaldehyde for 15 min and permeabilized with 0.1 % Triton X-100 for 10 min. After washing with PBS, the cells were blocked with 5 % BSA for 1 h at room temperature. They were then incubated with phalloidin conjugated to a fluorescent dye (TRITC, YEASON, China) at the recommended concentration for 30 min in the dark. After washing three times with PBS, the nuclei were counterstained with DAPI for 5 min. Fluorescence images were captured using a Confocal microscope.

4.18. Flow cytometry

Flow cytometry was utilized to characterize the polarization phenotype of the cultured Raw264.7 cells. Following the manufacturer's instructions, the collected cells were incubated in 1 % BSA for 30 min to minimize nonspecific binding. Subsequently, the cells were washed and incubated with purified antibodies against F4/80 (Biolegend, B25763, USA) and CD206 (Santa Cruze, SC-58986, USA) at 4 °C for 1 h in the dark, followed by two washes. Flow cytometric analysis was conducted using flow cytometry (BD Bioscience, USA). The data were analyzed using Flowjo software.

4.19. Angiogenesis-related research

Different scaffolds were immersed in cell culture medium for 24 h in advance, and this cell culture medium was collected for HUVECs cultivation, respectively. Then Matrigel (200 μL/well) was gelled in a 24-well culture plate to induce tube formation, and HUVECs were seeded on the plate for 4 h. Subsequently, AM reagent was used to stain cells, tube formation ability of HUVECs was assessed with a fluorescence microscope.

4.20. Animal experiments

The ethics of animal experimentation was approved by the Ethics Committee of Shanghai Sixth People's Hospital (DWLL2024-0984). In this study, 40 six-week-old rats were anesthetized using isoflurane gas. Circular holes measuring 5 mm in diameter and 1 mm in thickness were drilled on each side of their skulls, which were then filled with different hydrogels and sutured closed. Half of the rats were euthanized at six and twelve weeks for subsequent testing of cranial bone repair effects.

4.21. Micro-CT analysis

The rat calvarial samples were analyzed using micro-CT scans (Skyscan 1276, Bruker, German). The micro-CT was set at 70 kV and 200 μA, with an aluminum filter of 0.5 mm, and scanning was performed for all specimens. The scanned images were reconstructed using the Skyscan NRecon program. Following reconstruction, BV/TV, Tb.Th and DA were visualized and quantified at the region of interest using SkyScan CTAn and CTVol.

4.22. Immunofluorescences staining assay

The skull tissues were first decalcified in EDTA solution for 4 weeks, and then dehydrated by sucrose solution, respectively. Next, the samples were embedded in OCT and sectioned at 10 μm [72]. The slices were blocked in PBS solution supplemented with 10 % horse serum and 0.3 % Triton X-100 for 1 h, and then incubated with primary Runx2 antibody (GB115631, Servicebio, China) and COL-1 antibody (GB115707, Servicebio, China) overnight at 4 °C. Then the second antibodies and DAPI dyes were added under dark environments. Finally, the immunofluorescence images were observed by DMI6. The immunofluorescence staining method for CD86 (GB115630, Servicebio, China), CD206 (GB113497, Servicebio, China), and CD31 (GB120005, Servicebio, China) were the same as described above.

4.23. Bioinformatic analysis and statistics

Transcriptomics study was conducted using bulk RNA-sequencing. Total RNA was extracted from each group of hydrogel-treated cells. The quality control of total RNA samples was done by 2100 Expert Bioanalyzer (Agilent), and RNA sequencing was done by Illumina Hiseq2000 platform of Majorbio Biotech (Shanghai, China). The data were analyzed online by the I-Sanger cloud platform.

The analysis of the osteoblast single-cell RNA sequencing dataset from Ugur M. Ayturk, using the Broad Institute's Single Cell Portal (https://singlecell.broadinstitute.org/single_cell/study/SCP1337/single-cell-rna-seq-of-cultured-and-primary-mouse-calvarial-cells#study-visualize).

4.24. H&E staining and Masson staining

Decalcified samples were stained with H&E and Masson staining kits according to the manufacturer's instructions. Representative images were obtained using a microscope.

4.25. Statistical analysis

Data were representative of greater than three independent experiments. Statistical differences were determined by One-way ANOVA and

Tukey's multiple comparison test. Results were expressed as mean ± standard deviation (SD). The differences were regarded as statistically significant with *P < 0.05, **P < 0.01, ***P < 0.001 and ****P < 0.0001.

CRediT authorship contribution statement

Jianyang Shan: Writing – review & editing, Writing – original draft, Visualization, Validation, Methodology, Investigation, Formal analysis, Data curation, Conceptualization. **Liang Cheng:** Visualization, Validation, Methodology, Funding acquisition. **Xiang Li:** Visualization, Validation, Methodology, Investigation. **Wenhao Liu:** Visualization, Validation, Methodology. **Zhihua Liu:** Visualization, Validation, Methodology, Investigation. **Yimin Chai:** Validation, Supervision, Resources, Funding acquisition. **Yaling Yu:** Writing – review & editing, Validation, Supervision, Resources, Methodology, Funding acquisition, Conceptualization. **Xing Wang:** Writing – review & editing, Validation, Supervision, Resources, Methodology, Funding acquisition, Conceptualization. **Gen Wen:** Validation, Supervision, Resources, Project administration, Methodology, Funding acquisition, Conceptualization.

Data availability statement

The data that support the findings of this study are available from the corresponding author upon reasonable request.

Ethics approval and consent to participate

The Shanghai Sixth People's Hospital Affiliated to Shanghai Jiao Tong University School of Medicine Animal Welfare Ethics Committee has examined that the use of experimental animals and the experimental conditions and operation techniques of animal research in the "End-Tail Soaking Strategy Toward Robust and Biomimetic Sandwich-Layered Hydrogels for Full-Thickness Bone Regeneration" project carried out by the applicant's Department of Orthopaedics, Liu Wenhao, and its participants, Shan Jianyang, Li Xiang, Liu Zhihua, and Yu Yaling, are in line with the welfare of experimental animals and the ethical norms. We hereby certify that.

Animal Ethics Review Acceptance Number: DWLL2024-0984.

Animal experiment registration number: DWSY2023-0142.

Laboratory animals used in the project: SD rats.

Declaration of competing interest

The authors declare no competing interests.

Acknowledgements

This work was supported by the National Natural Science Foundation of China (52373162, 82002291 and 51973226), Beijing Natural Science Foundation (L244037), National Key R&D program of China (2020YFC2004906), and Key Program of National Natural Science Foundation of China (81930069).

Appendix ASupplementary data

Supplementary data to this article can be found online at https://doi.org/10.1016/j.bioactmat.2025.02.045.

References

[1] C. Xu, Z.Z. Liu, X. Chen, Y. Gao, W.J. Wang, X.J. Zhuang, H. Zhang, X.F. Dong, Bone tissue engineering scaffold materials: fundamentals, advances, and challenges, Chin. Chem. Lett. 35 (2) (2024) 109197.

[2] J. Lin, T. Huang, H. Wei, B. Bao, T. Gao, X. Zheng, H. Zhu, Does preoperative glycemic control restore immune defense against implant-related infection in mice with diabetes? Clin. Orthop. Relat. Res. 480 (5) (2022) 1008–1017.

[3] M. Saab, C. Zobrist, N. Blanchemain, B. Martel, F. Chai, Systematic literature review of in vivo rat femoral defect models using biomaterials to improve the induced membrane technique: a comprehensive analysis, EFORT Open Reviews 9 (2) (2024) 138–145.

[4] M. Rezapourian, I. Hussainova, Optimal mechanical properties of hydroxyapatite gradient voronoi porous scaffolds for bone applications - a numerical study, J. Mech. Behav. Biomed. Mater. 148 (2023) 106232.

[5] Q. Wang, J. Luan, Z. Zhao, W. Kong, C. Zhang, J. Ding, Dentin-desensitizing biomaterials, Chin. Chem. Lett. 34 (8) (2023) 108060.

[6] Y.C. Peng, Y.L. Zhuang, Y. Liu, H.X. Le, D. Li, M.R. Zhang, K. Liu, Y.B. Zhang, J. L. Zuo, J.X. Ding, Bioinspired gradient scaffolds for osteochondral tissue engineering, Explorations 3 (4) (2023) 20210043.

[7] J.Q. Chen, X.H. He, T.Y. Sun, K. Liu, C.H. Chen, W. Wen, S. Ding, M.X. Liu, C. R. Zhou, B.H. Luo, Highly elastic and anisotropic wood-derived composite scaffold with antibacterial and angiogenic activities for bone repair, Adv. Healthcare Mater. 12 (21) (2023) 2300122.

[8] Z.H. Fan, H.X. Liu, Z.Z. Ding, L.Y. Xiao, Q. Lu, D.L. Kaplan, Simulation of cortical and cancellous bone to accelerate tissue regeneration, Adv. Funct. Mater. 33 (33) (2023) 2301839.

[9] L.H. Fu, C. Qi, T.W. Sun, K. Huang, J. Lin, P. Huang, Glucose oxidase-instructed biomineralization of calcium-based biomaterials for biomedical applications, Explorations 3 (6) (2023) 20210110.

[10] T. Yang, Z. Hao, Z. Wu, B. Xu, J. Liu, L. Fan, Q. Wang, Y. Li, D. Li, S. Tang, C. Liu, W. Li, W. Teng, An engineered lamellar bone mimicking full-scale hierarchical architecture for bone regeneration, Bioact. Mater. 27 (2023) 181–199.

[11] N. Reznikov, M. Bilton, L. Lari, M.M. Stevens, R. Kroger, Fractal-like hierarchical organization of bone begins at the nanoscale, Science 360 (6388) (2018) eaao2189.

[12] X. Cai, H. Follet, L. Peralta, M. Gardegaront, D. Farlay, R. Gauthier, B. Yu, E. Gineyts, C. Olivier, M. Langer, A. Gourrier, D. Mitton, F. Peyrin, Q. Grimal, P. Laugier, Anisotropic elastic properties of human femoral cortical bone and relationships with composition and microstructure in elderly, Acta Biomater. 90 (2019) 254–266.

[13] L. Zhu, D. Luo, Y. Liu, Effect of the nano/microscale structure of biomaterial scaffolds on bone regeneration, Int. J. Oral Sci. 12 (1) (2020) 6.

[14] I.H. Parkinson, N.L. Fazzalari, Interrelationships between structural parameters of cancellous bone reveal accelerated structural change at low bone volume, J. Bone Miner. Res. 18 (12) (2003) 2200–2205.

[15] I.L. Ivanovska, J.W. Shin, J. Swift, D.E. Discher, Stem cell mechanobiology: diverse lessons from bone marrow, Trends Cell Biol. 25 (9) (2015) 523–532.

[16] J.H. He, G.B. Chen, M.Y. Liu, Z.L. Xu, H. Chen, L. Yang, Y.G. Lv, Scaffold strategies for modulating immune microenvironment during bone regeneration, Mater. Sci. Eng., C 108 (2020) 110411.

[17] R. Wazzani, S. Pallu, C. Bourzac, S. Ahmaïdi, H. Portier, C. Jaffré, Physical activity and bone vascularization: a way to explore in bone repair context? Life-Basel 11 (8) (2021) 783.

[18] L.Y. Liu, J. Wu, S.Y. Lv, D.L. Xu, S.J. Li, W.T. Hou, C. Wang, D.S. Yu, Synergistic effect of hierarchical topographic structure on 3D-printed titanium scaffold for enhanced coupling of osteogenesis and angiogenesis, Materials Today Bio 23 (2023) 100866.

[19] L.L. Yang, L. Ge, Q.H. Zhou, T. Mokabber, Y.T. Pei, R. Bron, P. van Rijn, Biomimetic multiscale hierarchical topography enhances osteogenic differentiation of human mesenchymal stem cells, Adv. Mater. Interfac. 7 (14) (2020) 2000385.

[20] J.C. Tang, Y. Gu, H.B. Zhang, L. Wu, Y. Xu, J.N. Mao, T.W. Xin, T.J. Ye, L.F. Deng, W.G. Cui, H.A. Santos, L. Chen, Outer-inner dual reinforced micro/nano hierarchical scaffolds for promoting osteogenesis, Nanoscale 11 (34) (2019) 15794–15803.

[21] D.X. Ke, J. Yu, P.X. Liu, C.M. Niu, X. Yang, Biomimetic 3D printed PCL/TCP/GelMA scaffolds with improved osteogenesis and angiogenesis for non-load bearing applications, Materialia 21 (2022) 101339.

[22] Y.H. Seo, S.H. Hwang, Y.N. Kim, H.J. Kim, E.B. Bae, J.B. Huh, Bone reconstruction using two-layer porcine-derived bone scaffold composed of cortical and cancellous bones in a rabbit calvarial defect model, Int. J. Mol. Sci. 23 (5) (2022) 2647.

[23] M.J. Zhang, T.T. Yu, J. Li, H.C. Yan, L. Lyu, Y. Yu, G.C. Yang, T. Zhang, Y.H. Zhou, X. Wang, D.W. Liu, Matrix metalloproteinase-responsive hydrogel with on-demand release of phosphatidylserine promotes bone regeneration through immunomodulation, Adv. Sci. 11 (20) (2024) 2306924.

[24] J.J. Diao, J. OuYang, T. Deng, X. Liu, Y.T. Feng, N.R. Zhao, C.B. Mao, Y.J. Wang, 3D-plotted beta-tricalcium phosphate scaffolds with smaller pore sizes improve in vivo bone regeneration and biomechanical properties in a critical-sized calvarial defect rat model, Adv. Healthcare Mater. 7 (17) (2018) 1800441.

[25] B. Sun, H.F. Wang, B. Xiao, H.C. Yan, H.Q. Wu, R.C. Zhang, Y. Zhang, W. Yuan, X. Wang, C.G. Shi, Bioactive composite hydrogel with effects of robust promoting osteogenesis and immunomodulation for osteoporotic bone regeneration, Chem. Eng. J. 476 (2023) 146743.

[26] T.T. Yu, L.Y. Zhang, X.Y. Dou, R.S. Bai, H.F. Wang, J. Deng, Y.F. Zhang, Q.N. Sun, Q. Li, X. Wang, B. Han, Mechanically robust hydrogels facilitating bone regeneration through epigenetic modulation, Adv. Sci. 9 (32) (2022) 2203734.

[27] Y.F. Zhang, X.Y. Dou, L.Y. Zhang, H.F. Wang, T. Zhang, R.S. Bai, Q.N. Sun, X. Wang, T.T. Yu, D.C. Wu, B. Han, X.L. Deng, Facile fabrication of a biocompatible composite gel with sustained release of aspirin for bone regeneration, Bioact. Mater. 11 (2022) 130–139.

[28] T. Almela, I.M. Brook, K. Khoshroo, M. Rasoulianboroujeni, F. Fahimipour, M. Tahriri, E. Dashtimoghadam, A. El-Awa, L. Tayebi, K. Moharamzadeh,

Simulation of cortico-cancellous bone structure by 3D printing of bilayer calcium phosphate-based scaffolds, Bioprinting 6 (2017) 1–7.
[29] J.M. Ringeard, P. Griesmar, E. Caplain, M. Michiel, S. Serfaty, J.Y. Le Huerou, D. Marinkova, L. Yotova, Design of poly(*N*-acryloylglycine) materials for incorporation of microorganisms, J. Appl. Polym. Sci. 130 (2) (2013) 835–841.
[30] C.Y. Cui, T.L. Wu, F. Gao, C.C. Fan, Z.Y. Xu, H.B. Wang, B. Liu, W.G. Liu, An autolytic high strength instant adhesive hydrogel for emergency self-rescue, Adv. Funct. Mater. 28 (42) (2018) 1804925.
[31] I.M. El-Sherbiny, Synthesis, characterization and metal uptake capacity of a new carboxymethyl chitosan derivative, Eur. Polym. J. 45 (1) (2009) 199–210.
[32] Z.Y. Wan, J.H. He, Y.T. Yang, T. Chong, J.X. Wang, B.L. Guo, L. Xue, Injectable adhesive self-healing biocompatible hydrogel for haemostasis, wound healing, and postoperative tissue adhesion prevention in nephron-sparing surgery, Acta Biomater. 152 (2022) 157–170.
[33] J.P. Gong, Y. Katsuyama, T. Kurokawa, Y. Osada, Double-network hydrogels with extremely high mechanical strength, Adv. Mater. 15 (14) (2003) 1155.
[34] Y.Y. Yang, X. Wang, D.C. Wu, Chitosan-based high-mechanical double-network hydrogels: construction, modulation and applications, Hua Hsueh Hsueh Pao 79 (1) (2021) 1–9.
[35] Y.Y. Yang, X. Wang, F. Yang, L.N. Wang, D.C. Wu, Highly elastic and ultratough hybrid ionic-covalent hydrogels with tunable structures and mechanics, Adv. Mater. 30 (18) (2018) 1707071.
[36] Y.R. Chen, X. Yan, F.Z. Yuan, L. Lin, S.J. Wang, J. Ye, J.Y. Zhang, M. Yang, D. C. Wu, X. Wang, J.K. Yu, Kartogenin-conjugated double-network hydrogel combined with stem cell transplantation and tracing for cartilage repair, Adv. Sci. 9 (35) (2022) 2105571.
[37] S.S. Wang, D.P. Wang, G.L. Wang, M.L. Zhang, Y.R. Sun, J.X. Ding, Antibacterial carbon dots, Materials Today Bio 30 (2025) 101383.
[38] N.D. da Costa, L.S. Lima, M.E.A. Galiciolli, D.H.F. Ribeiro, M.M. Ribeiro, G.D. J. Garica, I.S. Marcal, J.F.D. Silva, M.E. Pereira, C.S. Oliveira, I.C. Guiloski, Drug-induced osteoporosis and mechanisms of bone tissue regeneration through trace elements, J. Trace Elem. Med. Biol. 84 (2024) 127446.
[39] K.C. Ye, X.M. Zhang, L. Shangguan, X.D. Liu, X.S. Nie, Y.Q. Qiao, Manganese-implanted titanium modulates the crosstalk between bone marrow mesenchymal stem cells and macrophages to improve osteogenesis, J. Funct. Biomater. 14 (9) (2023) 456.
[40] R.M. Li, Z.Y. Zhu, B.L. Zhang, T. Jiang, C. Zhu, P. Mei, Y. Jin, R.Q. Wang, Y.X. Li, W.M. Guo, C.X. Liu, L.G. Xia, B. Fang, Manganese enhances the osteogenic effect of silicon-hydroxyapatite nanowires by targeting t lymphocyte polarization, Adv. Sci. 11 (4) (2024) 2305890.
[41] Z.H. Wu, Y.M. Sun, S.D. Mu, M.R. Bai, Q. Li, T. Ma, L. Ma, F. Chen, X.L. Luo, L. Ye, C. Cheng, Manganese-based antioxidase-inspired biocatalysts with axial mn-n^5 sites and 2d d-π-conjugated networks for rescuing stem cell fate, Angew. Chem. Int. Ed. 62 (22) (2023) e202302329.
[42] E. Mancuso, O.A. Bretcanu, M. Marshall, M.A. Birch, A.W. McCaskie, K. W. Dalgarno, Novel bioglasses for bone tissue repair and regeneration: effect of glass design on sintering ability, ion release and biocompatibility, Mater. Des. 129 (2017) 239–248.
[43] B. Yang, H. Yao, J. Yang, C. Chen, Y. Guo, H. Fu, J. Shi, In situ synthesis of natural antioxidase mimics for catalytic anti-inflammatory treatments: rheumatoid arthritis as an example, J. Am. Chem. Soc. 144 (1) (2022) 314–330.
[44] C. Sun, S.Q. Li, J.X. Ding, Biomaterials-boosted immunotherapy for osteosarcoma, Adv. Healthcare Mater. 13 (23) (2024) 2400864.
[45] Z.T. Liu, J. Zhang, C.F. Fu, J.X. Ding, Osteoimmunity-regulating biomaterials promote bone regeneration, Asian J. Pharm. Sci. 18 (1) (2023) 100774.
[46] M.A. Stranick, $Mn_2O_3$by XPS, Surf. Sci. Spectra 6 (1) (1999) 39–46.
[47] X.Y. Dou, H.F. Wang, F. Yang, H. Shen, X. Wang, D.C. Wu, One-step soaking strategy toward anti-swelling hydrogels with a stiff "armor", Adv. Sci. 10 (9) (2023) 2206242.
[48] M.K. Lee, H. Lee, C. Park, I.G. Kang, J. Kim, H.E. Kim, H.D. Jung, T.S. Jang, Accelerated biodegradation of iron-based implants via tantalum-implanted surface nanostructures, Bioact. Mater. 9 (2022) 239–250.
[49] S. Mandal, A. Kishore, S. Mandal, B. Bhar, B.B. Mandal, S.K. Nandi, M. Roy, Controlled nano Cu precipitation through age treatment: a method to enhance the biodegradation, mechanical, antimicrobial properties and biocompatibility of Fe-20Mn-3Cu alloys, Acta Biomater. 168 (2023) 650–669.
[50] J.M. Li, C.J. Deng, W.Y. Liang, F. Kang, Y. Bai, B. Ma, C.T. Wu, S.W. Dong, Mn-containing bioceramics inhibit osteoclastogenesis and promote osteoporotic bone regeneration via scavenging ros, Bioact. Mater. 6 (11) (2021) 3839–3850.
[51] P.L. Huang, G.J. Li, C.X. Chen, H. Wang, Y. Han, S.H. Zhang, Y. Xiao, M. Zhang, N. Liu, J.H. Chu, L. Zhang, Z.W. Sun, Differential toxicity of Mn^{2+} and Mn^{3+} to rat liver tissues: oxidative damage, membrane fluidity and histopathological changes, Exp. Toxicol. Pathol. 64 (3) (2012) 197–203.
[52] A.U. Khan, R.M. Qu, T.Y. Fan, J. Ouyang, J.X. Dai, A glance on the role of actin in osteogenic and adipogenic differentiation of mesenchymal stem cells, Stem Cell Res. Ther. 11 (1) (2020) 283.
[53] M.Y. Sun, G.F. Chi, J.J. Xu, Y. Tan, J.Y. Xu, S. Lv, Z.R. Xu, Y.H. Xia, L.S. Li, Y.L. Li, Extracellular matrix stiffness controls osteogenic differentiation of mesenchymal stem cells mediated by integrin α5, Stem Cell Res. Ther. 9 (2018) 52.
[54] H. Zhang, M. Zhang, D. Zhai, C. Qin, Y. Wang, J. Ma, H. Zhuang, Z. Shi, L. Wang, C. Wu, Polyhedron-like biomaterials for innervated and vascularized bone regeneration, Adv. Mater. 35 (42) (2023) e2302716.
[55] Y. Xu, C. Xu, H. Song, X. Feng, L. Ma, X. Zhang, G. Li, C. Mu, L. Tan, Z. Zhang, Z. Liu, Z. Luo, C. Yang, Biomimetic bone-periosteum scaffold for spatiotemporal regulated innervated bone regeneration and therapy of osteosarcoma, J. Nanobiotechnol. 22 (1) (2024) 250.
[56] C.G. Worley, D. Bombick, J.W. Allen, R.L. Suber, M. Aschner, Effects of manganese on oxidative stress in CATH.a cells, Neurotoxicology 23 (2) (2002) 159–164.
[57] I. Batinic-Haberle, Z. Rajic, L. Benov, A combination of two antioxidants (an SOD mimic and ascorbate) produces a pro-oxidative effect forcing escherichia coli to adapt via induction of oxyR regulon, Anti Cancer Agents Med. Chem. 11 (4) (2011) 329–340.
[58] S.M.A. Pinto, A.R.R. Ferreira, D.S.S. Teixeira, S.C.C. Nunes, A. de Carvalho, J.M. S. Almeida, Z. Garda, A. Pallier, A. Pais, C.M.A. Brett, E. Tóth, M.P.M. Marques, M. M. Pereira, C. Geraldes, Fluorinated Mn(III)/(II)-porphyrin with redox-responsive ^1H and ^{19}F relaxation properties, Chem.–Eur. J. 29 (53) (2023) e202301442.
[59] Z.R. He, C.H. Sun, Y.F. Ma, X. Chen, Y. Wang, K. Chen, F.R. Xie, Y. Zhang, Y. Yuan, C.S. Liu, Rejuvenating aged bone repair through multihierarchy reactive oxygen species-regulated hydrogel, Adv. Mater. 36 (9) (2024) 2306552.
[60] Q.X. Chen, J.Y. Li, F. Han, Q.C. Meng, H. Wang, W. Qiang, Z.X. Li, F.F. Li, E. Xie, X. Y. Qin, S. Chen, W.S. Wang, C.Y. Liu, B. Li, F.X. Han, A multifunctional composite hydrogel that rescues the ros microenvironment and guides the immune response for repair of osteoporotic bone defects, Adv. Funct. Mater. 32 (27) (2022) 2201067.
[61] X.R. Li, Y.H. Si, J.X. Liang, M.S. Li, Z.W. Wang, Y.Y. Qin, L.T. Sun, Enhancing bone regeneration and immunomodulation via gelatin methacryloyl hydrogel-encapsulated exosomes from osteogenic pre-differentiated mesenchymal stem cells, J. Colloid Interface Sci. 672 (2024) 179–199.
[62] M.L. Bouxsein, S.K. Boyd, B.A. Christiansen, R.E. Guldberg, K.J. Jepsen, R. Müller, Guidelines for assessment of bone microstructure in rodents using micro-computed tomography, J. Bone Miner. Res. 25 (7) (2010) 1468–1486.
[63] X.D. Wang, S.Y. Li, S.J. Zhang, A. Gupta, C.P. Zhang, L. Wang, The neural system regulates bone homeostasis via mesenchymal stem cells: a translational approach, Theranostics 10 (11) (2020) 4839–4850.
[64] H. Lee, G. Han, Y. Na, M. Kang, S.J. Bang, H.S. Kang, T.S. Jang, J.H. Park, H. L. Jang, K. Yang, H. Kang, H.D. Jung, 3D-printed tissue-specific nanospike-based adhesive materials for time-regulated synergistic tumor therapy and tissue regeneration in vivo, Adv. Funct. Mater. 34 (48) (2024) 2406237.
[65] M.M. Weivoda, E.W. Bradley, Macrophages and bone remodeling, J. Bone Miner. Res. 38 (3) (2023) 359–369.
[66] Y.W. Li, Q.J. Sheng, C. Zhang, C. Han, H. Bai, P.P. Lai, Y.X. Fan, Y. Ding, X.G. Dou, STAT6 up-regulation amplifies M2 macrophage anti-inflammatory capacity through mesenchymal stem cells, Int. Immunopharmacol. 91 (2021) 107266.
[67] Y. Zhang, S.N. Chen, X. Qin, A. Guo, K. Li, L.X. Chen, W.W. Yi, Z.L. Deng, F.R. Tay, W.B. Geng, L. Miao, Y. Jiao, B.L. Tao, A versatile chitosan-based hydrogel accelerates infected wound healing via bacterial elimination, antioxidation, immunoregulation, and angiogenesis, Adv. Healthcare Mater. 13 (19) (2024) 2400318.
[68] S.Q. Wang, Y.H. Liu, Q.W. Sun, B.W. Zeng, C. Liu, L.M. Gong, H. Wu, L.Q. Chen, M. J. Jin, J.P. Guo, Z.G. Gao, W. Huang, Triple cross-linked dynamic responsive hydrogel loaded with selenium nanoparticles for modulating the inflammatory microenvironment via PI3K/Akt/NF-kB and MAPK signaling pathways, Adv. Sci. 10 (31) (2023) 2303167.
[69] L. Li, Y.J. Liu, X.S. Qian, L. Zhou, Y.J. Fan, X. Yang, K. Luo, Y.L. Chen, Modulating the phenotype and function of bone marrow-derived macrophages via mandible and femur osteoblasts, Int. Immunopharmacol. 132 (2024) 112000.
[70] U.M. Ayturk, J.P. Scollan, D. Goz Ayturk, E.S. Suh, A. Vesprey, C.M. Jacobsen, P. Divieti Pajevic, M.L. Warman, Single-cell rna sequencing of calvarial and long-bone endocortical cells, J. Bone Miner. Res. 35 (10) (2020) 1981–1991.
[71] J. Lin, T. Gao, H. Wei, H. Zhu, X. Zheng, Optimal concentration of ethylenediaminetetraacetic acid as an irrigation solution additive to reduce infection rates in rat models of contaminated wound, Bone & Joint Research 10 (1) (2021) 68–76.
[72] J. Lin, W. Hu, T. Gao, B. Bao, X. Li, T. Huang, Y. Sun, J. Shen, H. Xu, K. Zhu, H. Zhu, Y. Yang, X. Zheng, ε-Poly-l-lysine as an efficient cartilage penetrating and residing drug carrier with high intraarticular injection safety for treating osteoarthritis, Chem. Eng. J. 430 (2022) 133018.